scientific reports

Check for updates

OPEN

Finite element investigation of TPMS-inspired microplate structures for mechanical stability enhancement in sports equipment

Long Liu[1], Jalil jamali[2]✉, Loke Kok Foong[3,4]✉ & Murat Yaylacı[5,6]

The development of lightweight but impact-resistant sports gear needs structural ideas that boost mechanical stability while also keeping good energy uptake characteristics. Here, we do a finite element look into TPMS inspired multilayer microplate designs under dynamic input, like real-time excitation. We choose three different TPMS cores, Primitive, Gyroid, and I-graph, wrapped into what we call a Wrapped Package-graph, to see how they affect the nonlinear vibration behavior and the energy dissipation in sandwich-type microplates. The mechanical setup is built on Mindlin–Reissner plate theory, but we also add von Kármán-style geometric nonlinearity, so the model can capture the moderate to large deflection effects properly. For size-related trends, we use the modified strain gradient theory (MSGT), in which several material length-scale parameters are brought in to represent microscale deformation mechanisms in a more faithful way. Furthermore, the way the microplate interacts with its supporting medium is treated through a nonlinear elastic foundation, so the behavior stays close to the more realistic operating conditions you see in sports equipment. A full finite element setup is built, where the nonlinear part of the deviatoric stretch-gradient vector is slipped into the governing equations. Then the nonlinear system is handled in order to pull out transient responses, mode shapes, and how kinetic, potential, and overall energies change in time. After that, parametric checks are run to see how the TPMS topology, the excitation intensity, the foundation stiffness, the geometric dimensions, and those MSGT length-scale parameters affect the structural performance. The numerical findings show clear gaps between the P, G, and IWP architectures when it comes to vibration behavior and the ability to absorb energy. Especially, TPMS-based multilayer microplates seem to provide better dynamic steadiness, together with a higher elastic strain energy, which suggests they could be used in next-generation high-performance sports hardware under impact and vibration loading.

Keywords TPMS, MSGT, Nonlinear dynamic analysis, Finite element method, Size-dependent sports equipment, Elastic strain energy

TPMS-based materials have lately attracted quite some interest within engineering, due to their unique geometric and mechanical properties[1]. The first important property is their complex repeating structure, which provides an unusually large surface-to-volume ratio – a highly desirable property for chemical catalysis, filtration, and heat transfer processes[2]. Another advantage of these materials is that they provide impressive mechanical strength for the minimum possible weight, which makes them attractive for aerospace engineering, automotive design, and biomedical implants[3]. The natural minimal surfaces of TPMS structures allow using a minimum amount of material in retaining load-bearing capability, thus reducing the weight of the object[4]. These materials are known for exceptional shock resistance, which helps to make protective gear, impact-resistant structures, and shock-absorbing constructions[5]. Furthermore, their porosity can be designed to a precise level, which is extremely helpful for making scaffolds for tissue growth and bone regeneration[6]. The mechanical properties of TPMS

[1]School of Health Care, Chongqing Preschool Education College, Chongqing 404047, China. [2]Department of Mechanical Engineering, Sho.C., Islamic Azad University, Shoushtar, Iran. [3]Institute of Research and Development, Duy Tan University, Da Nang, Vietnam. [4]School of Engineering & Technology, Duy Tan University, Da Nang, Vietnam. [5]Department of Civil Engineering, Recep Tayyip Erdogan University, 53100 Rize, Türkiye. [6]Turgut Kıran Maritime Facult, Recep Tayyip Erdogan University, 53900 Rize, Türkiye. ✉email: jalil.jamali@iau.ac.ir; lokekokfoong@duytan.edu.vn

lattices are independent of directionality since they behave similarly irrespective of the direction of applied loads[7]. Due to their open-cell construction, these lattice structures are ideal for allowing free flow of liquids, which makes them ideal for heat exchange and fluid transfer applications[8]. TPMS lattices can be manufactured using additive manufacturing techniques and therefore offer opportunities for rapid prototyping and customized design[9]. They possess the ability to perform several tasks simultaneously, such as thermal conductivity, electrical properties, and mechanical strength due to their flexible nature[10]. Lastly, the combination of functionality and aesthetic appeal increases their applications in architecture[11].

The finite element analysis has now become the benchmark simulation technique for determining the effective mechanical behavior of triply periodic minimal surface structures by employing numerical homogenization techniques that help in assessing the elastic stiffness, shear modulus, and Poisson's ratio in different topological types such as Primitive, Gyroid, Diamond, and I-WP[12]. The FE analyses of parametric studies have revealed the effect of relative density, topological cell shape, and gradation on the performance of TPMS lattice structures, indicating that the mechanical properties can be considerably optimized using appropriate design parameters[13]. Nonetheless, the simulation of TPMS structures is not an easy task due to the complex topologies, high surface-to-volume ratios, and the presence of highly nonlinear behavior due to large deformations and strain gradients experienced under dynamic loadings[14]. Higher-order continuum theory-based FE formulations, particularly the modified strain gradient theory, have been proposed for addressing the stiffening behavior at the micro-plate scale where the classical continuum mechanics theory is unable to account for such behavior[15].

The process of additive manufacturing has brought about an innovation in the field of engineering design as far as the production of complex designs is concerned. Additive manufacturing allows for the production of materials in a highly efficient manner, and topology optimization and lattice infilling have been seen as techniques which can help produce high-performance parts with increased efficiencies[16]. TPMS heat sinks have attracted a lot of interest as far as their application in microprocessors as advanced coolers are concerned. Gyroid and diamond designs have shown superior heat dissipation characteristics owing to high surface area to volume ratio and optimized fluid flow characteristics[17]. Optimization of design parameters and orientation of parts during 3D printing have helped in producing optimal components with high mechanical properties and reduced defects[18]. Also, optimization of Ti-6Al-4 V has helped in reducing mass and increasing stiffness and frequency of parts[19].

The proper analysis of microplates as essential elements in MEMS devices, micro-sensors, and aerospace micro-structures requires going beyond the scope of classical continuum mechanics since experiments show that whenever the dimension of a structure gets close to the intrinsic microstructure length scale of a material, then size effect arises and becomes evident in the form of the "smaller is stiffer" effect[20]. In order to properly analyze these scale-dependent effects, various non-classical continuum theories have been proposed, such as the strain gradient theory, couple stress theory, surface energy theory, and nonlocal gradient elasticity theory[21]. The MSGT can be considered one of the most reliable theories in this context because it introduces three different material length-scale parameters accounting for dilatation gradient, deviatoric stretch gradient, and rotation gradient effects[22].

A recent improved MSGT analysis indicated that increasing such length scale parameters increases the natural frequency and decreases the deflection of the microplates, where the structure Primitive TPMS has higher stiffness than any other topological shape[22]. Modified couple stress theory (MCST), which involves only one small-scale material length parameter, has been widely used in the investigation of functionally graded microplates under static bending, buckling, and free vibration, and the results indicate an increase in the stiffness, decrease in deflections, and increase in the natural frequencies with consideration of size effects[23]. Recently, MCST has been applied in more complicated systems like rotating polycrystalline silicon microplates, where the presence of size dependency results in higher natural frequencies, but lower dynamic response, as well as non-linear behaviors that depend on the rotational velocity and aspect ratio[24]. Nonlocal strain gradient theory (NSGT), based on Eringen's nonlocal elasticity model and strain gradient effects, can consider both stiffness hardening and softening behaviors due to the use of multiple length-scale parameters, and it has been used in the study of thermoelastic damping and wave propagation in functionally graded microplates with reinforcement of carbon nanotubes and graphene platelets[25,26].

Recently, there has been a unified DQFE formulation for size-dependent vibration analysis of layered microplates considering elastic boundary conditions using a combination of MCST and a two-variable shear deformation theory under the influence of a Winkler-Pasternak elastic foundation[20]. However, although there have been several advancements in this domain, the formulation of a unified theory that is capable of incorporating various higher-order continuum theories, length scale material constants, and the coupling effects of multiple physical fields is still an active area of research[27]. Dynamic analysis of TPMS microstructures has recently become one of the most important topics of research due to the mathematical topology, outstanding mechanical properties, and practical applications of such structures in novel lightweight engineering systems[28]. It is necessary to know the features of free vibrations, transient dynamics, and dynamic instabilities of such complicated structures in order to successfully apply them in the aerospace industry, automotive sector, and biomedicine[29]. The finite element method and modern isogeometric analysis have become the most common methods for studying the dynamics of TPMS microplates and making accurate predictions of the natural frequencies and modes of motion and nonlinear transient dynamics[30]. Nevertheless, classical continuum mechanics cannot describe the size effects which become significant when the dimensions of the microplate become comparable with the intrinsic length-scale parameters of the material, which makes it necessary to use the theory of higher-order continua[31].

Despite the significant advances made in the investigation of the properties of cellular structures derived from TPMS and their size-dependent microplate mechanical behavior, the nonlinear dynamic response of multilayer TPMS microplates subjected to dynamic excitations still needs further examination, especially in the case of

high-performance sports equipment, which requires effective vibration damping and increased elastic strain energy storage abilities. Furthermore, the interaction between various TPMS geometries and size-dependent higher-order linear elasticities, nonlinearities of geometry, and nonlinear foundation has not yet been analyzed in one computational model. To bridge the knowledge gap, the current research proposes a new finite element formulation for multilayer microplates using the core structure composed of P, G, and IWP TPMS geometries. The formulation is developed based on the theory of Mindlin-Reissner plates, nonlinear von Kármán geometry, modified strain gradient elasticity with several material length scales, as well as the nonlinear influence of the deviatoric stretch-gradient vector. Three main novelties in this study can be distinguished: (i) the design of the size-dependent nonlinear finite element model for modeling the coupled effect of TPMS topology and microscale on the dynamic stability; (ii) the first systematic comparison of P, G, and IWP TPMS core configurations for multilayer microplates under dynamic loading and nonlinear elastic foundation interaction; and (iii) the evaluation of the mode shapes, kinetic, potential, and total transient energies as well as absorbed energy capacity to determine the optimal TPMS core configurations for high impact resistant and vibration tolerant sport equipment. The obtained results contribute new knowledge about designing lightweight, mechanically stable, and energy-efficient TPMS structures for mechanically resilient sport components where vibration damping is required. It should be noted that this study covers only mechanical properties and dynamic behavior of TPMS microplates, but does not consider any optical and electrical characteristics of TPMS structures. Thermal mismatch, electrical shorting, and optical shading are not taken into account in this study. It is worth noting that the present work is theoretical and numerical, and it deals only with the mechanical dynamic behavior of TPMS microplates. No optical, electrical, or experimental PV characterization is considered in this work.

Mathematical modeling

The modeling process involves four consecutive stages: (i) effective properties of the TPMS through homogenization ("Modeling of triply periodic minimal surface" subsection); (ii) kinematics and strain definitions ("Fundamental equations" subsection); (iii) strain gradient constitutive relation and potential energy; (iv) finite elements formulation and assembling ("Finite element formulation" subsection). In this way, it becomes evident how each assumption affects the system matrices. Figure 1 demonstrates the three-dimensional geometry of the TPMS-inspired microplate under the influence of the external dynamic load. The microplate geometry is considered as the rectangular microplate with sizes a and b that define the geometrical in-plane lengths along the y- and x-axis, respectively. In order to characterize the spatial deformation and displacement field of the microplate, the $x-y-z$ Cartesian coordinate system is defined, where z-axis corresponds to the thickness direction of the microplate. The external excitation is described with the parameter of the Ω_{ext} acting downward on the top surface of the plate. This configuration is used as the geometrical basis of the finite element analysis of the nonlinear vibration behavior, stability, and energy dissipation of the TPMS-based multilayer microplate used in sports equipment.

The multilayer structure of the TPMS-based microplate and its response to the nonlinear elastic foundation are demonstrated in Fig. 2. As shown in this Fig., the microplate comprises three major layers: a metal contact layer at the top, a TPMS layer, and a metal contact layer at the bottom. The overall thickness of the microplate is represented by h and is decomposed into three individual layer thicknesses, namely h_1, h_2, and h_3. Specifically, h_1 stands for the thickness of the bottom metal contact layer, h_2 stands for the thickness of the TPMS layer, and h_3 stands for the thickness of the top metal contact layer. In the present case, the TPMS layer serves as the lightweight core structure that provides stiffness enhancement, improved vibration damping, and energy dissipation capabilities, whereas the metallic layers serve as the external protection and load-transferring elements. The multilayer microplate is subjected to an external excitation, acting along the vertical direction at the top surface, that simulates the dynamic impact or vibrations. The microplate is mounted on a nonlinear elastic foundation that comprises a substrate and distributed elastic springs. The stiffness parameters of the foundation are presented by k_p, k_w, and k_3. k_p stands for the stiffness generated due to the coupling between the microplate and the top supporting medium, k_w stands for the stiffness of the intermediate nonlinear spring foundation that provides vertical elastic resistance, and k_3 stands for the stiffness of the bottom substrate foundation. The coordinate system has been established such that x-axis is the axis along the length of the plate while z-axis is the

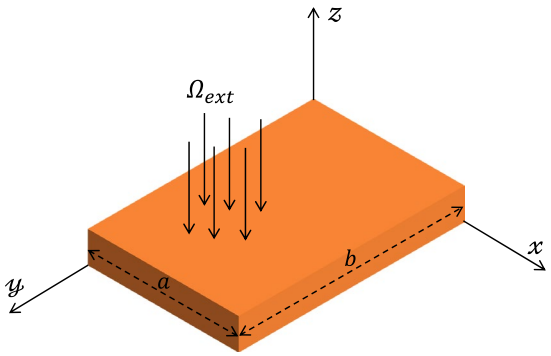


Fig. 1. The geometric configuration of the TPMS-inspired microplate under external excitation.

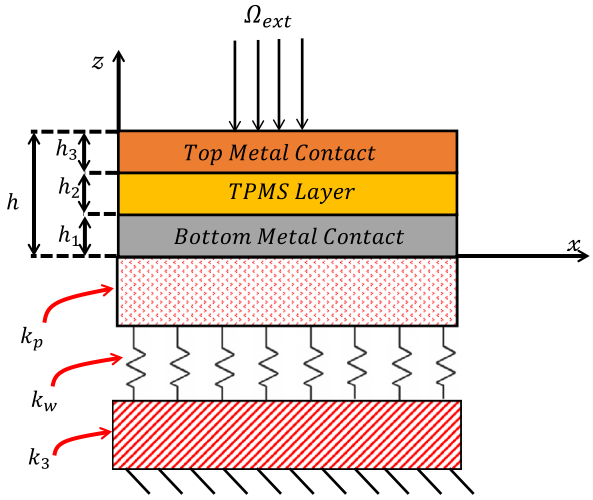


Fig. 2. The multilayer composition of the TPMS-inspired microplate surrounded by a nonlinear elastic foundation.

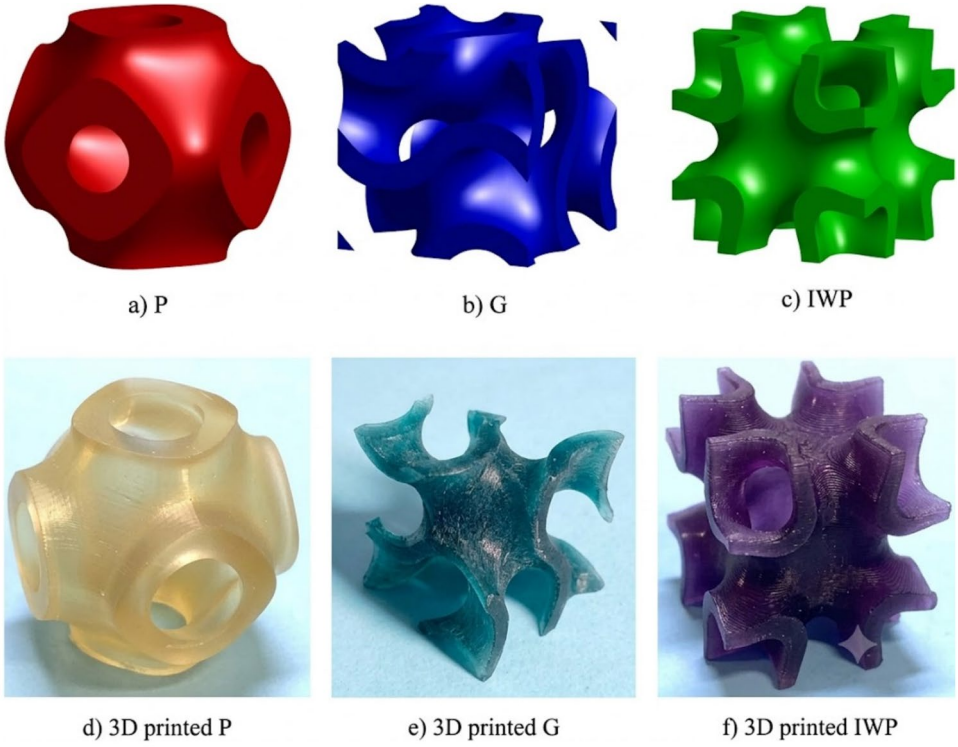


Fig. 3. Across the layer depth of the graded composite panels, a schematic view to display the layout of the cellular TPMS architectures[32].

axis along the thickness of the plate, which helps in expressing the mathematical description of the multilayer microplate deformation and vibration responses.

Modeling of triply periodic minimal surface

In the present study, three distinct types of triply periodic minimal surface configurations—namely the Primitive (P), Gyroid (G), and I-graph with Wrapped Package-graph (IWP)—are considered for the foundation layer, as depicted in Fig. 3.

To estimate the mechanical behavior of these intricate architectures via computational models, Ref [33]. introduced an effective medium approach that provides approximate values for three fundamental material

properties. The formulas given below allow one to compute the elastic stiffness, rigidity under shear, and lateral contraction ratio for the three types of sheet-based TPMS configurations.

$$\frac{E(\rho)}{E_b} = \begin{cases} C_1^E \rho^{n_1^E}, & \rho \le k_m^E \\ C_2^E \rho^{n_2^E} + C_3^E. & \rho > k_m^E \end{cases}, \tag{1a}$$

$$\frac{G(\rho)}{G_b} = \begin{cases} C_1^G \rho^{n_1^G}, & \rho \le k_m^G \\ C_2^G \rho^{n_2^G} + C_3^G. & \rho > k_m^G \end{cases}, \tag{1b}$$

$$\nu(\rho) = \begin{cases} a_1 e^{(b_1 \rho)} + d_1, & \rho \le k_\nu \\ a_2 \rho^2 + b_2 \rho + d_2. & \rho > k_\nu \end{cases}. \tag{1c}$$

In this context, the symbols E_b and G_b denote the elastic stiffness and the shear rigidity of the underlying solid material. The normalized density, defined as the ratio $\rho(x)/\rho_b$ where ρ_b is the density of the base substance, appears in the preceding relations. The specific coefficients for each TPMS topology, as introduced in Eqs. (1a–1c), are compiled in Table 1 and further elaborated through Eqs. (2a–2d).

$$C_1^E \left(k_m^E\right)^{n_1^E} = C_2^E \left(k_m^E\right)^{n_2^E} + C_3^E, \tag{2a}$$

$$C_2^E + C_3^E = 1, \tag{2b}$$

$$a_1 e^{b_1 k_\nu} + d_1 = 0.3, \tag{2c}$$

$$a_2 k_\nu^2 + b_2 k_\nu + d_2 = 0.3, \tag{2d}$$

$$a_2 + b_2 + d_2 = 0.3. \tag{2e}$$

In this investigation, two distinct schemes of void fraction variation are considered through the depth of the material, in connection with the graded mass distribution of the TPMS architectures. The mathematical definitions for these two porosity layouts are provided below[33]:

$$PatternPA : \rho = \rho_{min} + (\rho_{max} - \rho_{min}) \left(\frac{1}{2} + \frac{x - h_1 - \frac{h_2}{2}}{h_2}\right)^{n_A}, \tag{3a}$$

$$PatternPB : \rho = \rho_{min} + (\rho_{max} - \rho_{min}) \left(1 - cos\left(\pi \frac{x - h_1 - \frac{h_2}{2}}{h_2}\right)\right)^{n_B}. \tag{3b}$$

The homogenized TPMS properties assume ideal periodic connectivity and fully bonded struts; manufacturing imperfections may reduce absolute stiffness but do not alter the topology ranking. The exponent n_i determines how the void fraction changes through the plate's depth, with the relative density bounded between ρ_{min} and ρ_{max}. The specific exponent values for the two porosity distribution models employed here are listed below, as taken from Ref [34].

Property	Parameter	TPMS type		
		P	G	IWP
Elastic modulus, E (GPa)	C_1^E	0.317	0.596	0.597
	n_1^E	1.264	1.467	1.225
	n_2^E	2.006	2.351	1.782
	k_m^E	0.25	0.45	0.35
Shear modulus, G (GPa)	C_1^G	0.705	0.777	0.529
	n_1^G	1.189	1.544	1.287
	n_2^G	1.715	1.982	2.188
	k_m^G	0.25	0.45	0.35
Poisson's ratio, ν	a_1	0.314	0.192	2.597
	b_1	−1.004	−1.349	−0.157
	a_2	0.152	0.402	0.201
	k_ν	0.55	0.50	0.13

Table 1 . The governing coefficients used to describe the structural response across the distinct TPMS families.

Parameter	PA1	PA2	PA3	PB1	PB2	PB3
ρ_{min}	0.2	0.2	0.25	0.2	0.2	0.25
ρ_{max}	0.5	0.5	1.0	0.5	0.8	1.0
$n_A(n_B)$	1.0	3.0	6.5	0.561	1.757	3.943

Table 2. Detailed values for six density distributions.

Layey	Material	h	E	ρ	ν
1	Lower metallic face-sheet	$150[nm]$	$83[GPa]$	10490	0.37
2	FG-TPMS	$50[\mu m]$	E_1	ρ_1	ν_1
3	Upper metallic face-sheet	$70[nm]$	$200[GPa]$	3170	0.28

Table 3. A list of the characteristics of the materials in the fabrication of the presented structure[36].

$$n_A = \frac{\rho_{\max} - \frac{M}{\rho_s h_2}}{\frac{M}{\rho_s h_2} - \rho_{\min}}, \tag{4a}$$

$$\frac{M}{\rho_b h_2} = \int_0^1 \frac{2\rho_{\max}\left(1 - \rho_0 + \rho_0 (1-u)^{n_B}\right)}{\pi\sqrt{1-u^2}} du, \tag{4b}$$

Clamped and simply supported edges bracket practical sports fastenings (rigid bonding vs compliant straps), ensuring the predicted trends remain conservative and valid for real mounting variability. In which $\rho_0 = 1 - \frac{\rho_{\min}}{\rho_{\max}}$ and $u = cos\left(\pi \frac{^{s}-h_1-\frac{h_2}{2}}{h_2}\right)$. Moreover, the mass distributed over a unit surface area designated by the quantity M is obtained through the following relation.

$$M = \int_{h_1}^{h_1+h_2} \rho(Z)\, dZ \tag{5}$$

This part presents the computational findings obtained for the FG-TPMS plates. Unless stated otherwise, the solid constituent is taken to be stainless steel SUS304, characterized by an elastic modulus of 207.79 GPa, a density of 8166 kg/m^3, and a Poisson's ratio of 0.3. Since the TPMS architecture is made from a single homogeneous material, its coefficient of thermal expansion is identical to that of the bulk solid, as noted in reference[33]. The specific parameter values relevant to the present conditions, derived from Eq. (4), are summarized in Table 2 [35].

The characteristics of the constituent materials used to fabricate the latest generation of the presented structure are summarized in Table 3.

For other TPMS topologies and density patterns, effective properties vary as per Eqs. (1)–(4); parametric variations are systematically examined in "Parametric results" section.

Fundamental equations

Strain gradient model

The change in elastic deformation potential, according to the MSGT framework established by Lam and colleagues[37], is expressed in the following manner.

$$\delta U = \frac{1}{2}\int_V (\sigma_{ij}\delta\varepsilon_{ij} + p_i\delta\xi_i + \tau_{ijk}\delta\kappa_{ijk} + m_{ij}\delta\mathfrak{G}_{ij})dV. \tag{6}$$

In this context, the expressions for the gradient components covering the volumetric deformation measure (ξ_i), the rotational gradient fields ($\mathfrak{G}_{ij}$), the standard deformation tensor (ε_{ij}), and the deviatoric distortion gradient (κ_{ijk}) are given below

$$\varepsilon_{ij} = \frac{1}{2}\left(u_{i,j} + u_{j,i} + u_{k,i}u_{k,j}\right), \tag{7a}$$

$$\begin{aligned}\kappa_{ijk} =& \frac{1}{3}\left(\varepsilon_{ij,k} + \varepsilon_{jk,i} + \varepsilon_{ki,j}\right) - \frac{1}{15}\delta_{ij}\left(\varepsilon_{mm,k} + 2\varepsilon_{mk,m}\right) \\ &- \frac{1}{15}\left[\delta_{jk}\left(\varepsilon_{mm,i} + 2\varepsilon_{mi,m}\right) + \delta_{ki}\left(\varepsilon_{mm,j} + 2\varepsilon_{mj,m}\right)\right],\end{aligned} \tag{7b}$$

$$\mathfrak{G}_{ij} = \frac{1}{4}\left(e_{imn}u_{n,mj} + e_{jmn}u_{n,mi}\right), \tag{7c}$$

$$\xi_i = \varepsilon_{mm,i}. \tag{7d}$$

The kinematic state of the continuum is characterized by the field quantities denoted u_i. Once the two conventional elasticity coefficients (λ and μ) and the three internal length-scale parameters (l_0, l_1, l_2) from the MSG framework are introduced, the collection of traction-type tensors, namely the ordinary force-stress σ_{ij} together with its generalized higher-order counterparts τ_{ijk}, m_{ij}, p_i can be written in the following form

$$\sigma_{ij} = \lambda\varepsilon_{kk}\delta_{ij} + 2\mu\varepsilon_{ij}, \tag{8a}$$

$$\tau_{ijk} = 2\mu l_1^2\kappa_{ijk}, \tag{8b}$$

$$m_{ij} = 2\mu l_2^2\mathfrak{G}_{ij}, \tag{8c}$$

$$p_i = 2\mu l_0^2\xi_i. \tag{8d}$$

MSGT is adopted here because the TPMS core's ligament diameters (typically 10–100 μm) are comparable to the intrinsic material length scales, causing non-negligible size-dependent stiffening during high-strain-rate impacts. For SUS304, we adopt $l_0 = l_1 = l_2 = 0.3{-}1.0\mu m$ consistent with metallic microstructure experiments. This is critical for sports protective plates, where impact loads generate steep local deformation gradients at the cellular level; classical theory would underpredict local rigidity and distort transient energy dissipation predictions.

Mindlin- Reissner plate theory

We begin the mathematical formulation by adopting the kinematic framework of the Mindlin–Reissner plate model. Under this approach, the plate's deformation state is fully captured by defining the in-plane shifts (u, v, w) at the middle surface together with the two cross-sectional rotations ($\mathcal{F}, \mathcal{G}$).

$$u_x = u\left(x,y\right) + z\mathcal{F}\left(x,y\right), \tag{9a}$$

$$u_y = v\left(x,y\right) + z\mathcal{G}\left(x,y\right), \tag{9b}$$

$$u_z = w\left(x,y\right). \tag{9c}$$

Applying the von Kármán-type geometric nonlinearity along with Eqs. (9a) through (9c), the strain components that account for large deflections are defined in the following form

$$\mathcal{E} = \left\{ \begin{array}{c} \mathcal{E}_x \\ \mathcal{E}_y \\ \gamma_{xy} \end{array} \right\} = \mathcal{E}_0 + \mathcal{E}_{nl} + z\mathcal{E}_1, \tag{10a}$$

$$\left\{ \begin{array}{c} \gamma_{yz} \\ \gamma_{xz} \end{array} \right\} = \boldsymbol{\gamma}_0. \tag{10b}$$

with

$$\mathcal{E}_0 = \left\{ \begin{array}{c} u_{,x} \\ v_{,y} \\ u_{,y} + v_{,x} \end{array} \right\}, \mathcal{E}_{nl} = \left\{ \begin{array}{c} \frac{1}{2}w_{,x}w_{,x} \\ \frac{1}{2}w_{,y}w_{,y} \\ w_{,x}w_{,y} \end{array} \right\}, \mathcal{E}_1 = \left\{ \begin{array}{c} \mathcal{F}_{,x} \\ \mathcal{G}_{,y} \\ \mathcal{F}_{,y} + \mathcal{G}_{,x} \end{array} \right\}, \boldsymbol{\gamma}_0 = \left\{ \begin{array}{c} w_{,y} + G \\ w_{,x} + F \end{array} \right\}. \tag{11}$$

Subsequently, making use of Eq. (7b), the deviatoric component of the stretch-gradient vector is obtained as follows.

$$\boldsymbol{\kappa} = \boldsymbol{\kappa}_0 + \boldsymbol{\kappa}_{nl} + z\boldsymbol{\kappa}_1, \tag{12a}$$

$$\boldsymbol{\kappa} = \left\{ \begin{array}{c} \kappa_{xxx} \\ \kappa_{yyy} \\ \kappa_{xxx} \\ \kappa_{xxy} \\ \kappa_{xxx} \\ \kappa_{xyy} \\ \kappa_{xyx} \\ \kappa_{xxx} \\ \kappa_{yyx} \\ \kappa_{yxx} \end{array} \right\}, \boldsymbol{\kappa}_0 = \left\{ \begin{array}{c} \frac{1}{5}(2u_{,xx} - u_{,yy} - 2v_{,xy}) \\ \frac{1}{5}(-2u_{,xy} + 2v_{,yy} - v_{,xx}) \\ -\frac{1}{5}(w_{,xx} + w_{,yy} + 2\mathcal{F}_{,x} + 2\mathcal{G}_{,y}) \\ \frac{1}{15}(8u_{,xy} + 4v_{,xx} - 3v_{,yy}) \\ \frac{1}{15}(4w_{,xx} - w_{,yy} + 8\mathcal{F}_{,x} - 2\mathcal{G}_{,y}) \\ \frac{1}{15}(4u_{,yy} - 3u_{,xx} + 8v_{,xy}) \\ \frac{1}{3}(w_{,xy} + \mathcal{F}_{,y} + \mathcal{G}_{,x}) \\ -\frac{1}{15}(3u_{,xx} + u_{,yy} + 2v_{,xy}) \\ \frac{1}{15}(4w_{,yy} - w_{,xx} - 2\mathcal{F}_{,x} + 8\mathcal{G}_{,y}) \\ -\frac{1}{15}(2u_{,xy} + v_{,xx} - 3v_{,yy}) \end{array} \right\}, \tag{12b}$$

$$\boldsymbol{\kappa}_{nl}=\left\{\begin{array}{c}\frac{1}{5}(2w_{,x}w_{,xx}-w_{,x}w_{,yy}-2w_{,y}w_{,xy})\\ \frac{1}{5}(-2w_{,x}w_{,xy}+2w_{,y}w_{,yy}-w_{,y}w_{,xx})\\ 0\\ \frac{1}{15}(8w_{,x}w_{,xy}+4w_{,y}w_{,xx}-3w_{,y}w_{,yy})\\ 0\\ \frac{1}{15}(4w_{,x}w_{,yy}-3w_{,x}w_{,xx}+8w_{,y}w_{,xy})\\ 0\\ -\frac{1}{15}(3w_{,x}w_{,xx}+w_{,x}w_{,yy}+2w_{,y}w_{,xy})\\ 0\\ -\frac{1}{15}(2w_{,x}w_{,xy}+w_{,y}w_{,xx}-3w_{,y}w_{,yy})\end{array}\right\},\tag{12c}$$

$$\boldsymbol{\kappa}_{1}=\left\{\begin{array}{c}\frac{1}{5}(2\mathcal{F}_{,xx}-\mathcal{F}_{,yy}-2\mathcal{G}_{,xy})\\ \frac{1}{5}(-2\mathcal{F}_{,xy}-\mathcal{G}_{,xx}+2\mathcal{G}_{,yy})\\ 0\\ \frac{1}{15}(8\mathcal{F}_{,xy}+4\mathcal{G}_{,xx}-3\mathcal{G}_{,yy})\\ 0\\ \frac{1}{15}(-3\mathcal{F}_{,xx}+4\mathcal{F}_{,yy}+8\mathcal{G}_{,xy})\\ 0\\ -\frac{1}{15}(3\mathcal{F}_{,xx}+\mathcal{F}_{,yy}+2\mathcal{G}_{,xy})\\ 0\\ -\frac{1}{15}(2\mathcal{F}_{,xy}+\mathcal{G}_{,xx}+3\mathcal{G}_{,yy})\end{array}\right\}.\tag{12d}$$

Proceeding in a parallel fashion, the vector for the rotation gradient is expressed through Eq. (7c) in the form below.

$$\mathfrak{A}=\mathfrak{A}_0+{}_x\mathfrak{A}_1,\tag{13a}$$

$$\mathfrak{A}=\left\{\begin{array}{c}\mathfrak{A}_{xx}\\ \mathfrak{A}_{yy}\\ \mathfrak{A}_{xy}\\ \mathfrak{A}_{yx}\\ \mathfrak{A}_{zx}\\ \mathfrak{A}_{zy}\end{array}\right\},\mathfrak{A}_0=\left\{\begin{array}{c}\frac{1}{2}(w_{,xy}-\mathcal{G}_{,x})\\ \frac{1}{2}(-w_{,xy}+\mathcal{F}_{,y})\\ \frac{1}{4}(w_{,yy}-w_{,xx}+\mathcal{F}_{,x}-\mathcal{G}_{,y})\\ \frac{1}{2}(-\mathcal{F}_{,y}+\mathcal{G}_{,x})\\ \frac{1}{4}(-u_{,xy}+v_{,xx})\\ \frac{1}{4}(-u_{,yy}+v_{,xy})\end{array}\right\},\mathfrak{A}_1=\left\{\begin{array}{c}0\\ 0\\ 0\\ 0\\ \frac{1}{4}(-\mathcal{F}_{,xy}+\mathcal{G}_{,xx})\\ \frac{1}{4}(-\mathcal{F}_{,yy}+\mathcal{G}_{,xy})\end{array}\right\}.\tag{13b}$$

Furthermore, the nonlinear dilatation-gradient vector is obtained by employing Eq. (7d) in the following manner.

$$\boldsymbol{\xi}=\boldsymbol{\xi}_0+\boldsymbol{\xi}_{nl}+{}_x\boldsymbol{\xi}_1,\tag{14a}$$

$$\boldsymbol{\xi}=\left\{\begin{array}{c}\xi_x\\ \xi_y\\ \xi_z\end{array}\right\},\boldsymbol{\xi}_0=\left\{\begin{array}{c}u_{,xx}+v_{,xy}\\ u_{,xy}+v_{,yy}\\ \mathcal{F}_{,x}+\mathcal{G}_{,y}\end{array}\right\},\boldsymbol{\xi}_{nl}=\left\{\begin{array}{c}w_{,x}w_{,xx}+w_{,y}w_{,xy}\\ w_{,x}w_{,xy}+w_{,y}w_{,yy}\\ 0\end{array}\right\},\boldsymbol{\xi}_1=\left\{\begin{array}{c}\mathcal{F}_{,xx}+\mathcal{G}_{,xy}\\ \mathcal{F}_{,xy}+\mathcal{G}_{,yy}\\ 0\end{array}\right\}.\tag{14b}$$

By applying the relations given in Eqs. (8a) through (8d) within the MSGM framework, the resulting expressions for the force–stress and the associated higher-order traction vectors are written in the following form.

$$\boldsymbol{\sigma}^b=\left\{\begin{array}{c}\sigma_x\\ \sigma_y\\ \sigma_{xy}\end{array}\right\}=\frac{E}{1-\nu^2}\left[\begin{array}{ccc}1&\nu&0\\ \nu&1&0\\ 0&0&\frac{1-\nu}{2}\end{array}\right]\left\{\begin{array}{c}\mathcal{E}_x\\ \mathcal{E}_y\\ \gamma_{xy}\end{array}\right\}=\mathbf{C}^b\mathcal{E},\tag{15a}$$

$$\boldsymbol{\sigma}^s=\left\{\begin{array}{c}\sigma_{yx}\\ \sigma_{xx}\end{array}\right\}=\frac{E}{2(1+\nu)}\left[\begin{array}{cc}1&0\\ 0&1\end{array}\right]\left\{\begin{array}{c}\gamma_{yx}\\ \gamma_{xx}\end{array}\right\}=\mathbf{C}^s\boldsymbol{\gamma}_0.\tag{15b}$$

And

$$\boldsymbol{\tau}=[\tau_{xxx}\tau_{yyy}\tau_{xxx}\tau_{xxy}\tau_{zxx}\tau_{zyy}\tau_{zyx}\tau_{zxx}\tau_{yyx}\tau_{yyx}]^T=2\mu l_1^2\boldsymbol{\kappa},\tag{16a}$$

$$m=[m_{xx}m_{yy}m_{xy}m_{xx}m_{xx}m_{yx}]^T=2\mu l_2^2\mathfrak{A},\tag{16b}$$

$$\mathbf{p}=\left\{\begin{array}{c}p_x\\ p_y\\ p_z\end{array}\right\}=2\mu l_0^2\boldsymbol{\xi}.\tag{16c}$$

Additionally, considering the previous expressions, the force and moment resultants of the conventional type are defined as follows.

$$\left\{\begin{array}{c}n^c\\ m^c\\ \mathcal{E}\end{array}\right\}=\left[\begin{array}{ccc}\mathcal{A}^c&0&0\\ 0&\mathcal{D}^c&0\\ 0&0&\overline{\mathcal{A}}^c\end{array}\right]\left(\left\{\begin{array}{c}\mathcal{E}_0\\ \mathcal{E}_1\\ \boldsymbol{\gamma}_0\end{array}\right\}+\frac{1}{2}\left\{\begin{array}{c}\mathcal{E}_{nl}\\ 0\\ 0\end{array}\right\}\right)=\widetilde{\mathcal{D}}^c\left(\widetilde{\mathcal{E}}+\frac{1}{2}\widetilde{\mathcal{E}}_{nl}\right),\tag{17}$$

The generalized traction resultants of the extended type are defined accordingly.

$$\left\{ \begin{array}{c} \mathscr{n}^{\xi} \\ \mathscr{m}^{\xi} \end{array} \right\} = \left[\begin{array}{cc} \mathcal{A}^{\xi} \boldsymbol{I}_{3\times 3} & 0 \\ 0 & \mathcal{D}^{\xi} \boldsymbol{I}_{3\times 3} \end{array} \right] \left(\left\{ \begin{array}{c} \boldsymbol{\xi}_0 \\ \boldsymbol{\xi}_1 \end{array} \right\} + \left\{ \begin{array}{c} \boldsymbol{\xi}_{nl} \\ 0 \end{array} \right\} \right) = \widetilde{\mathcal{D}}^{\xi} \left(\widetilde{\boldsymbol{\xi}} + \widetilde{\boldsymbol{\xi}}_{nl} \right), \tag{18a}$$

$$\left\{ \begin{array}{c} \mathscr{n}^{\kappa} \\ \mathscr{m}^{\kappa} \end{array} \right\} = \left[\begin{array}{cc} \mathcal{A}^{\kappa} \boldsymbol{I}_{10\times 10} & 0 \\ 0 & \mathcal{D}^{\kappa} \boldsymbol{I}_{10\times 10} \end{array} \right] \left(\left\{ \begin{array}{c} \boldsymbol{\kappa}_0 \\ \boldsymbol{\kappa}_1 \end{array} \right\} + \left\{ \begin{array}{c} \boldsymbol{\kappa}_{nl} \\ 0 \end{array} \right\} \right) = \widetilde{\mathcal{D}}^{\kappa} \left(\widetilde{\boldsymbol{\kappa}} + \widetilde{\boldsymbol{\kappa}}_{nl} \right), \tag{18b}$$

$$\left\{ \begin{array}{c} \mathscr{n}^{\mathfrak{A}} \\ \mathscr{m}^{\mathfrak{A}} \end{array} \right\} = \left[\begin{array}{cc} \mathcal{A}^{\mathfrak{A}} \boldsymbol{I}_{10\times 10} & 0 \\ 0 & \mathcal{D}^{\mathfrak{A}} \boldsymbol{I}_{10\times 10} \end{array} \right] \left\{ \begin{array}{c} \mathfrak{A}_0 \\ \mathfrak{A}_1 \end{array} \right\} = \widetilde{\mathcal{D}}^{\mathfrak{A}} \widetilde{\mathfrak{A}}. \tag{18c}$$

where

$$\mathcal{A}^{c} = \int_0^h \mathcal{C}^{b} d_{\mathscr{x}} = \int_0^{h_1} \mathcal{C}^{b1} d_{\mathscr{x}} + \int_{h_1}^{h_1+h_2} \mathcal{C}^{b2} d_{\mathscr{x}} + \int_{h_1+h_2}^{h} \mathcal{C}^{b3} d_{\mathscr{x}}, \tag{19a}$$

$$\mathcal{D}^{c} = \int_0^h \mathcal{C}^{b} {}_{\mathscr{x}}{}^{2} d_{\mathscr{x}} = \int_0^{h_1} {}_{\mathscr{x}}{}^{2} \mathcal{C}^{b1} d_{\mathscr{x}} + \int_{h_1}^{h_1+h_2} {}_{\mathscr{x}}{}^{2} \mathcal{C}^{b2} d_{\mathscr{x}} + \int_{h_1+h_2}^{h} {}_{\mathscr{x}}{}^{2} \mathcal{C}^{b3} d_{\mathscr{x}}, \tag{19b}$$

$$\overline{\mathcal{A}}^{c} = k_s \int_0^h \mathcal{C}^{s} d_{\mathscr{x}} = k_s \int_0^{h_1} \mathcal{C}^{s1} d_{\mathscr{x}} + k_s \int_{h_1}^{h_1+h_2} \mathcal{C}^{s2} d_{\mathscr{x}} + k_s \int_{h_1+h_2}^{h} \mathcal{C}^{s3} d_{\mathscr{x}}, \tag{19c}$$

$$\left(\mathcal{A}^{\xi}, \mathcal{D}^{\xi} \right) = \int_0^h 2\mu l_0^2 \left(1, {}_{\mathscr{x}}{}^{2} \right) d_{\mathscr{x}} = \int_0^{h_1} 2\mu_1 l_0^2 \left(1, {}_{\mathscr{x}}{}^{2} \right) d_{\mathscr{x}} + \int_{h_1}^{h_1+h_2} 2\mu_2 l_0^2 \left(1, {}_{\mathscr{x}}{}^{2} \right) d_{\mathscr{x}} + \int_{h_1+h_2}^{h} 2\mu_3 l_0^2 \left(1, {}_{\mathscr{x}}{}^{2} \right) d_{\mathscr{x}}, \tag{19d}$$

$$\left(\mathcal{A}^{\kappa}, \mathcal{D}^{\kappa} \right) = \int_0^h 2\mu l_1^2 \left(1, {}_{\mathscr{x}}{}^{2} \right) d_{\mathscr{x}} = \int_0^{h_1} 2\mu_1 l_1^2 \left(1, {}_{\mathscr{x}}{}^{2} \right) d_{\mathscr{x}} + \int_{h_1}^{h_1+h_2} 2\mu_2 l_1^2 \left(1, {}_{\mathscr{x}}{}^{2} \right) d_{\mathscr{x}} + \int_{h_1+h_2}^{h} 2\mu_3 l_1^2 \left(1, {}_{\mathscr{x}}{}^{2} \right) d_{\mathscr{x}}, \tag{19e}$$

$$\left(\mathcal{A}^{\mathfrak{A}}, \mathcal{D}^{\mathfrak{A}} \right) = \int_0^{h_1} 2\mu_1 l_0^2 \left(1, {}_{\mathscr{x}}{}^{2} \right) d_{\mathscr{x}} + \int_{h_1}^{h_1+h_2} 2\mu_2 l_0^2 \left(1, {}_{\mathscr{x}}{}^{2} \right) d_{\mathscr{x}} + \int_{h_1+h_2}^{h} 2\mu_3 l_0^2 \left(1, {}_{\mathscr{x}}{}^{2} \right) d_{\mathscr{x}}. \tag{19f}$$

It should be noted that the shear adjustment factor is taken as $k_s = 5/6$. Moreover, the interaction with the surrounding medium is represented by a nonlinear elastic support that includes a linear Winkler layer, a Pasternak shearing layer, and an additional cubic stiffness term. Accordingly, by applying the variational principle of Hamilton[38–40] together with the present formulation, the total energy expression for the microplate becomes the following.

$$\begin{aligned} &\int_{\Omega} \delta \left(\widetilde{\mathcal{E}} + \frac{1}{2} \widetilde{\mathcal{E}}_{nl} \right)^{T} \widetilde{\mathcal{D}}^{c} \left(\widetilde{\mathcal{E}} + \frac{1}{2} \widetilde{\mathcal{E}}_{nl} \right) d\Omega \\ &+ \int_{\Omega} \delta \left(\widetilde{\boldsymbol{\xi}} + \widetilde{\boldsymbol{\xi}}_{nl} \right)^{T} \widetilde{\mathcal{D}}^{\xi} \left(\widetilde{\boldsymbol{\xi}} + \widetilde{\boldsymbol{\xi}}_{nl} \right) d\Omega \\ &+ \int_{\Omega} \delta (\widetilde{\boldsymbol{\kappa}} + \widetilde{\boldsymbol{\kappa}}_{nl})^{T} \widetilde{\mathcal{D}}^{\kappa} \mathcal{Y}^{\kappa} \left(\widetilde{\boldsymbol{\kappa}} + \widetilde{\boldsymbol{\kappa}}_{nl} \right) d\Omega \\ &+ \int_{\Omega} \delta \widetilde{\mathfrak{A}}^{T} \widetilde{\mathcal{D}}^{\mathfrak{A}} \mathcal{Y}^{\mathfrak{A}} \widetilde{\mathfrak{A}} d\Omega \\ &+ \int_{\Omega} \delta \mathbf{U}^{T} \mathscr{m} \ddot{\mathbf{U}} d\Omega \\ &+ \int_{\Omega} k_w \mathscr{w} \delta \mathscr{w} d\Omega + \int_{\Omega} k_p \left(\mathscr{w}_{,\mathscr{x}} \delta \mathscr{w}_{,\mathscr{x}} + \mathscr{w}_{,\mathscr{y}} \delta \mathscr{w}_{,\mathscr{y}} \right) d\Omega \\ &+ \int_{\Omega} k_3 \mathscr{w}^{3} \delta \mathscr{w} d\Omega = \int_{\Omega} f \delta \mathscr{w} d\Omega. \end{aligned} \tag{20}$$

Let the displacement field be represented by the vector $\mathbf{U} = [\mathscr{w} \mathcal{F} \mathcal{G} \mathscr{w}]^{T}$. The mechanical behavior of the elastic foundation is governed by three distinct parameters: the linear stiffness coefficient of the Winkler layer (k_w), the shearing resistance of the Pasternak medium (k_p), and a cubic nonlinearity constant (k_3) that accounts for the nonlinear elastic response of the surrounding environment. The explicit forms of the terms $\mathcal{Y}^{\kappa}$, $\mathcal{Y}^{\mathfrak{A}}$, and the inertia parameter m are provided separately below.

$$\mathcal{Y}^{\kappa} = \begin{bmatrix} \overline{\mathcal{Y}}^{\kappa} & 0 \\ 0 & \overline{\mathcal{Y}}^{\kappa} \end{bmatrix}, diag\left(\overline{\mathcal{Y}}^{\kappa}\right) = [1113336111], \tag{21a}$$

$$\mathcal{Y}^{\mathfrak{A}} = \begin{bmatrix} \overline{\mathcal{Y}}^{\mathfrak{A}} & 0 \\ 0 & \overline{\mathcal{Y}}^{\mathfrak{A}} \end{bmatrix}, diag\left(\overline{\mathcal{Y}}^{\mathfrak{A}}\right) = [112122], \tag{21b}$$

$$\mathcal{m} = \int_0^{h_1} \rho_1 \begin{bmatrix} 1 & 0 & 0 & 0 & 0 \\ 0 & 1 & 0 & 0 & 0 \\ 0 & 0 & \mathcal{x}^2 & 0 & 0 \\ 0 & 0 & 0 & \mathcal{x}^2 & 0 \\ 0 & 0 & 0 & 0 & 1 \end{bmatrix} d\mathcal{x} + \int_{h_1}^{h_1+h_2} \rho_2 \begin{bmatrix} 1 & 0 & 0 & 0 & 0 \\ 0 & 1 & 0 & 0 & 0 \\ 0 & 0 & \mathcal{x}^2 & 0 & 0 \\ 0 & 0 & 0 & \mathcal{x}^2 & 0 \\ 0 & 0 & 0 & 0 & 1 \end{bmatrix} d\mathcal{x} + \int_{h_1+h_2}^{h} \rho_3 \begin{bmatrix} 1 & 0 & 0 & 0 & 0 \\ 0 & 1 & 0 & 0 & 0 \\ 0 & 0 & \mathcal{x}^2 & 0 & 0 \\ 0 & 0 & 0 & \mathcal{x}^2 & 0 \\ 0 & 0 & 0 & 0 & 1 \end{bmatrix} d\mathcal{x}. \tag{21c}$$

where ρ indicates the mass density.

Finite element formulation

The governing variational statement (Eq. 20) cannot be solved directly due to the spatially distributed displacement field. Therefore, the Hermitian shape functions (Eqs. 22–23) discretize the displacement vector into nodal degrees of freedom. This discretization transforms the continuous energy integrals into elemental matrix operators (Eqs. 24–33), which are assembled to yield system matrices for inertia, linear stiffness, damping, and nonlinear foundation. The final assembled equation (Eq. 39) is then solved in the time domain. This sequence systematically converts the continuous variational form into a discrete, solvable system. To address the present boundary-value problem, the finite element method is employed, following the standard procedures outlined in Refs.[41,42]. Accordingly, this section is devoted to the detailed development of the FE discretization. Given the presence of second-order spatial derivatives within the energy functional, a four-node Hermitian rectangular element is chosen to represent the unknown displacement field, making use of the interpolation functions defined below[43].

$$\mathcal{m}_i = \frac{1}{16}\left(2 + 3\mathfrak{a}_i\mathfrak{a} - \mathfrak{a}_i\mathfrak{a}^3\right)\left(2 + 3\mathfrak{b}_i\mathfrak{b} - \mathfrak{b}_i\mathfrak{b}^3\right), \tag{22a}$$

$$\hat{\mathcal{m}}_i = \frac{l_{\mathcal{x}}}{16}\left(-\mathfrak{a}_i - \mathfrak{a} + \mathfrak{a}_i\mathfrak{a}^2 + \mathfrak{a}^3\right)\left(2 + 3\mathfrak{b}_i\mathfrak{b} - \mathfrak{b}_i\mathfrak{b}^3\right), \tag{22b}$$

$$\check{\mathcal{m}}_i = \frac{l_{\mathcal{y}}}{16}\left(-\mathfrak{b}_i - \mathfrak{b} + \mathfrak{b}_i\mathfrak{b}^2 + \mathfrak{b}^3\right)\left(2 + 3\mathfrak{a}_i\mathfrak{a} - \mathfrak{a}_i\mathfrak{a}^3\right), \tag{22c}$$

$$\widetilde{\mathcal{m}}_i = \frac{l_{\mathcal{x}}l_{\mathcal{y}}}{16}\left(-\mathfrak{b}_i - \mathfrak{b} + \mathfrak{b}_i\mathfrak{b}^2 + \mathfrak{b}^3\right)\left(-\mathfrak{a}_i - \mathfrak{a} + \mathfrak{a}_i\mathfrak{a}^2 + \mathfrak{a}^3\right)(i = 1,2,3,4). \tag{22d}$$

The dimensionless variables a and b correspond respectively to the local coordinates along the global $\mathcal{x}$ and $\mathcal{y}$ axes, while $l_{\mathcal{x}}$ and $l_{\mathcal{y}}$ denote the side lengths of the element in those two directions. The quantities $\mathfrak{a}_i$ and $\mathfrak{b}_i$ represent the local coordinate values at each of the element's four nodes. Using this setup, the displacement vector $\mathcal{U} = [\mathcal{m}\mathcal{F}\mathcal{G}\mathcal{w}]^T$ is then expressed through the interpolation scheme given below[43].

$$\mathcal{U} = \sum_{i=1}^{4} \mathcal{m}_i \mathbf{d}_i = \mathcal{m}\mathbf{d}, \tag{23a}$$

$$\mathcal{m}_i = \begin{bmatrix} \mathcal{m}^i & 0 & 0 & 0 & 0 & \hat{\mathcal{m}}^i & 0 & 0 & 0 & 0 & \widetilde{\mathcal{m}}^i & 0 & 0 & 0 & 0 \\ 0 & \mathcal{m}^i & 0 & 0 & 0 & 0 & \hat{\mathcal{m}}^i & 0 & 0 & 0 & 0 & \widetilde{\mathcal{m}}^i & 0 & 0 & 0 \\ 0 & 0 & \mathcal{m}^i & 0 & 0 & 0 & 0 & \hat{\mathcal{m}}^i & 0 & 0 & 0 & 0 & \widetilde{\mathcal{m}}^i & 0 & 0 \\ 0 & 0 & 0 & \mathcal{m}^i & 0 & 0 & 0 & 0 & \hat{\mathcal{m}}^i & 0 & 0 & 0 & 0 & \widetilde{\mathcal{m}}^i & 0 \\ 0 & 0 & 0 & 0 & \mathcal{m}^i & 0 & 0 & 0 & 0 & \hat{\mathcal{m}}^i & 0 & 0 & 0 & 0 & \widetilde{\mathcal{m}}^i \end{bmatrix}, \tag{23b}$$

Subsequently, the computed contributions to the total deformation from both the primary (infinitesimal) and secondary (large-displacement) effects are written in the following form.

$$\widetilde{\mathcal{E}} = \begin{Bmatrix} \mathcal{E}_0 \\ \mathcal{E}_1 \\ \gamma_0 \end{Bmatrix} = \sum_{i=1}^{4} \begin{Bmatrix} \mathbf{B}_0^{\mathcal{E}} \\ \mathbf{B}_1^{\mathcal{E}} \\ \mathbf{B}_0^{\gamma} \end{Bmatrix}_i \mathbf{d}_i = \mathbf{B}^{\mathcal{E}}\mathbf{d}, \tag{24a}$$

$$\mathcal{E}_{nl} = \sum_{i=1}^{4} \mathbf{\Theta}_i^{\mathcal{E}} \mathbf{B}_{nl\,i}^{\mathcal{E}} \mathbf{d}_i = \mathbf{B}_{nl}^{\mathcal{E}}\mathbf{d}. \tag{24b}$$

Also, have

$$b_{0\,i}^{E} = \begin{bmatrix} n_{,x}^i & 0 & 0 & 0 & 0 & \hat{n}_{,x}^i & 0 & 0 & 0 & 0 & \check{n}_{,x}^i & 0 & 0 & 0 & 0 & \widetilde{n}_{,x}^i & 0 & 0 & 0 & 0 \\ 0 & n_{,y}^i & 0 & 0 & 0 & 0 & \hat{n}_{,y}^i & 0 & 0 & 0 & 0 & \check{n}_{,y}^i & 0 & 0 & 0 & 0 & \widetilde{n}_{,y}^i & 0 & 0 & 0 \\ n_{,y}^i & n_{,x}^i & 0 & 0 & 0 & \hat{n}_{,y}^i & \hat{n}_{,x}^i & 0 & 0 & 0 & \check{n}_{,y}^i & \check{n}_{,x}^i & 0 & 0 & 0 & \widetilde{n}_{,y}^i & \widetilde{n}_{,x}^i & 0 & 0 & 0 \end{bmatrix}, \tag{25a}$$

$$b^{E}_{1\,i}=\left[\begin{array}{ccccc ccccc ccccc ccccc}
0&0&n^{i}_{,x}&0&0&0&0&\hat{n}^{i}_{,x}&0&0&0&0&\check{n}^{i}_{,x}&0&0&0&0&\widetilde{n}^{i}_{,x}&0&0\\
0&0&0&n^{i}_{,y}&0&0&0&0&\hat{n}^{i}_{,y}&0&0&0&0&\check{n}^{i}_{,y}&0&0&0&0&\widetilde{n}^{i}_{,y}&0\\
0&0&n^{i}_{,y}&n^{i}_{,x}&0&0&0&\hat{n}^{i}_{,y}&\hat{n}^{i}_{,x}&0&0&0&\check{n}^{i}_{,y}&\check{n}^{i}_{,x}&0&0&0&\widetilde{n}^{i}_{,y}&\widetilde{n}^{i}_{,x}&0
\end{array}\right], \tag{25b}$$

$$b^{\gamma}_{0\,i}=\left[\begin{array}{ccccc ccccc ccccc ccccc}
0&0&n^{i}&0&n^{i}_{,x}&0&0&\hat{n}^{i}&0&\hat{n}^{i}_{,x}&0&0&\check{n}^{i}&0&\check{n}^{i}_{,x}&0&0&\widetilde{n}^{i}&0&\widetilde{n}^{i}_{,x}\\
0&0&0&n^{i}&n^{i}_{,y}&0&0&0&\hat{n}^{i}&\hat{n}^{i}_{,y}&0&0&0&\check{n}^{i}&\check{n}^{i}_{,y}&0&0&0&\widetilde{n}^{i}&\widetilde{n}^{i}_{,y}
\end{array}\right], \tag{25c}$$

$$b^{E}_{nl\,i}=\left[\begin{array}{ccccc ccccc ccccc ccccc}
0&0&0&0&n^{i}_{,x}&0&0&0&0&\hat{n}^{i}_{,x}&0&0&0&0&\check{n}^{i}_{,x}&0&0&0&0&\widetilde{n}^{i}_{,x}\\
0&0&0&0&n^{i}_{,y}&0&0&0&0&\hat{n}^{i}_{,y}&0&0&0&0&\check{n}^{i}_{,y}&0&0&0&0&\widetilde{n}^{i}_{,y}
\end{array}\right], \tag{25d}$$

$$\boldsymbol{\Theta}^{\mathscr{E}}_{i}=\left[\begin{array}{cc}
w_{,x}&0\\
0&w_{,y}\\
w_{,y}&w_{,x}
\end{array}\right]. \tag{25e}$$

Following that, an approximate representation is obtained for the linear part as well as the nonlinear part of the deviatoric stretch-gradient vector.

$$\widetilde{\boldsymbol{\kappa}}=\left\{\begin{array}{c}\boldsymbol{\kappa}_0\\ \boldsymbol{\kappa}_1\end{array}\right\}=\sum_{i=1}^{4}\left\{\begin{array}{c}\mathscr{b}^{\kappa}_{0}\\ \mathscr{b}^{\kappa}_{1}\end{array}\right\}_{i}\mathbf{d}_i=\mathscr{b}^{\kappa}\mathbf{d}, \tag{26a}$$

$$\widetilde{\boldsymbol{\kappa}}_{nl}=\sum_{i=1}^{4}\boldsymbol{\Theta}^{\kappa}_{i}\,\mathscr{b}^{\kappa}_{nl\,i}\mathbf{d}_{\,i}=\mathscr{b}^{\kappa}_{nl}\mathbf{d}, \tag{26b}$$

With

$$b^{\kappa}_{0i}=\left[e^{\kappa}_{0i}\hat{e}^{\kappa}_{0i}e^{\kappa}_{0i}\tilde{e}^{\kappa}_{0i}\right], \tag{27a}$$

$$b^{\kappa}_{1i}=\left[e^{\kappa}_{1i}\hat{e}^{\kappa}_{1i}\check{e}^{\kappa}_{1i}\widetilde{e}^{\kappa}_{1i}\right], \tag{27b}$$

in which the matrix operators $\mathscr{a}^{\kappa}_{0\,i}$ and $\mathscr{a}^{\kappa}_{1\,i}$ are expressed as

$$\mathscr{a}^{\kappa}_{0\,i}=\frac{1}{15}\left[\begin{array}{ccccc}
6n^{i}_{,xx}-3n^{i}_{,yy}&-6n^{i}_{,xy}&0&0&0\\
-6n^{i}_{,xy}&6n^{i}_{,yy}-3n^{i}_{,xx}&0&0&0\\
0&0&-6n^{i}_{,x}&-6n^{i}_{,y}&-3(n^{i}_{,xx}+n^{i}_{,yy})\\
8n^{i}_{,xy}&4n^{i}_{,xx}-3n^{i}_{,yy}&0&0&0\\
0&0&8n^{i}_{,x}&-2n^{i}_{,y}&4n^{i}_{,xx}-n^{i}_{,yy}\\
4n^{i}_{,yy}-3n^{i}_{,xx}&8n^{i}_{,xy}&0&0&0\\
0&0&5n^{i}_{,y}&5n^{i}_{,x}&5n^{i}_{,xy}\\
-3n^{i}_{,xx}-n^{i}_{,yy}&-2n^{i}_{,xy}&0&0&0\\
0&0&-2n^{i}_{,x}&8n^{i}_{,y}&-n^{i}_{,xx}+4n^{i}_{,yy}\\
-2n^{i}_{,xy}&-n^{i}_{,xx}-3n^{i}_{,yy}&0&0&0
\end{array}\right], \tag{28a}$$

$$\mathscr{a}^{\kappa}_{1\,i}=\frac{1}{15}\left[\begin{array}{ccccc}
0&0&6n^{i}_{,xx}-3n^{i}_{,yy}&-6n^{i}_{,xy}&0\\
0&0&-6n^{i}_{,xy}&6n^{i}_{,yy}-3n^{i}_{,xx}&0\\
0&0&0&0&0\\
0&0&8n^{i}_{,xy}&4n^{i}_{,xx}-3n^{i}_{,yy}&0\\
0&0&0&0&0\\
0&0&-3n^{i}_{,xx}&4n^{i}_{,yy}+8n^{i}_{,xy}&0\\
0&0&0&0&0\\
0&0&-3n^{i}_{,xx}-n^{i}_{,yy}&-2n^{i}_{,xy}&0\\
0&0&0&0&0\\
0&0&-2n^{i}_{,xy}&-n^{i}_{,xx}-3n^{i}_{,yy}&0
\end{array}\right], \tag{28b}$$

$$\mathscr{b}^{\kappa}_{nl\,i}=\left[\begin{array}{ccccc ccccc ccccc ccccc}
0&0&0&0&n^{i}_{,xx}&0&0&0&0&\hat{n}^{i}_{,xx}&0&0&0&0&\check{n}^{i}_{,xx}&0&0&0&0&\widetilde{n}^{i}_{,xx}\\
0&0&0&0&n^{i}_{,yy}&0&0&0&0&\hat{n}^{i}_{,yy}&0&0&0&0&\check{n}^{i}_{,yy}&0&0&0&0&\widetilde{n}^{i}_{,yy}\\
0&0&0&0&n^{i}_{,xy}&0&0&0&0&\hat{n}^{i}_{,xy}&0&0&0&0&\check{n}^{i}_{,xy}&0&0&0&0&\widetilde{n}^{i}_{,xy}
\end{array}\right], \tag{28c}$$

$$\boldsymbol{\Theta}^{\kappa}_{i}=\frac{1}{15}\left[\begin{array}{ccc}
6w_{,x}&-3w_{,x}&-6w_{,y}\\
-3w_{,y}&6w_{,y}&-6w_{,x}\\
0&0&0\\
4w_{,y}&-3w_{,y}&8w_{,x}\\
0&0&0\\
-3w_{,x}&4w_{,x}&8w_{,y}\\
0&0&0\\
-3w_{,x}&-w_{,x}&-2w_{,y}\\
0&0&0\\
-w_{,y}&-w_{,y}&-2w_{,x}
\end{array}\right]. \tag{28d}$$

The remaining coefficient matrices appearing in Eqs. (27a) and (27b) are obtained by replacing $\mathscr{n}^i$ with their modified forms, namely $\hat{n}^i$, $\check{n}^i$ and $\tilde{n}^i$. In the same vein, inserting Eq. (23a) into Eqs. (13a) and (13b) yields the estimates for the rotational gradient vector, which are presented below.

$$\widetilde{\mathfrak{A}} = \left\{ \begin{array}{c} \mathfrak{A}_0 \\ \mathfrak{A}_1 \end{array} \right\} = \sum_{i=1}^{4} \left\{ \begin{array}{c} \mathscr{o}_0^{\mathfrak{A}} \\ \mathscr{o}_1^{\mathfrak{A}} \end{array} \right\}_i \mathbf{d}_i = \mathscr{o}^{\mathfrak{A}} \mathbf{d}, \tag{29}$$

With

$$\mathscr{o}_{0i}^{\mathfrak{A}} = \left[\begin{array}{cccc} \mathscr{o}_{0i}^{\mathfrak{A}} & \hat{\mathscr{o}}_{0i}^{\mathfrak{A}} & \check{\mathscr{o}}_{0i}^{\mathfrak{A}} & \tilde{\mathscr{o}}_{0i}^{\mathfrak{A}} \end{array} \right], \tag{30a}$$

$$\mathscr{o}_{1i}^{\mathfrak{A}} = \left[\begin{array}{cccc} \mathscr{o}_{1i}^{\mathfrak{A}} & \hat{\mathscr{o}}_{1i}^{\mathfrak{A}} & \check{\mathscr{o}}_{1i}^{\mathfrak{A}} & \tilde{\mathscr{o}}_{1i}^{\mathfrak{A}} \end{array} \right], \tag{30b}$$

where the matrix operators $\mathscr{o}_{0\,i}^{\mathfrak{A}}$ and $\mathscr{o}_{1\,i}^{\mathfrak{A}}$ are

$$\mathscr{o}_{0\,i}^{\mathfrak{A}} = \frac{1}{4} \left[\begin{array}{ccccc} 0 & 0 & 0 & -2\mathscr{n}_{,x}^{i} & 2\mathscr{n}_{,xy}^{i} \\ 0 & 0 & 2\mathscr{n}_{,y}^{i} & 0 & -2\mathscr{n}_{,xy}^{i} \\ 0 & 0 & \mathscr{n}_{,x}^{i} & -\mathscr{n}_{,y}^{i} & \mathscr{n}_{,yy}^{i} - \mathscr{n}_{,xx}^{i} \\ 0 & 0 & -2\mathscr{n}_{,y}^{i} & 2\mathscr{n}_{,x}^{i} & 0 \\ -\mathscr{n}_{,xy}^{i} & \mathscr{n}_{,xx}^{i} & 0 & 0 & 0 \\ -\mathscr{n}_{,yy}^{i} & \mathscr{n}_{,xy}^{i} & 0 & 0 & 0 \end{array} \right], \tag{31a}$$

$$\mathscr{o}_{1\,i}^{\mathfrak{A}} = \frac{1}{4} \left[\begin{array}{ccccc} 0 & 0 & 0 & 0 & 0 \\ 0 & 0 & 0 & 0 & 0 \\ 0 & 0 & 0 & 0 & 0 \\ 0 & 0 & 0 & 0 & 0 \\ 0 & 0 & -\mathscr{n}_{,xy}^{i} & \mathscr{n}_{,xx}^{i} & 0 \\ 0 & 0 & -\mathscr{n}_{,yy}^{i} & \mathscr{n}_{,xy}^{i} & 0 \end{array} \right]. \tag{31b}$$

The remaining matrix quantities that appear in Eqs. (30a) and (30b) are obtained through the replacement of the original parameter n^i by its three variants, respectively designated as $\hat{n}^i$, $\check{n}^i$ and $\tilde{n}^i$. In addition, the gradient contributions corresponding to the linear and nonlinear volumetric strains are expressed as follows.

$$\widetilde{\boldsymbol{\xi}} = \left\{ \begin{array}{c} \boldsymbol{\xi}_0 \\ \boldsymbol{\xi}_1 \end{array} \right\} = \sum_{i=1}^{4} \left\{ \begin{array}{c} \mathscr{o}_0^{\mathfrak{a}} \\ \mathscr{o}_1^{\mathfrak{a}} \end{array} \right\}_i \mathbf{d}_i = \mathscr{o}^{\mathfrak{a}} \mathbf{d}, \tag{32a}$$

$$\boldsymbol{\xi}_{nl} = \sum_{i=1}^{4} \boldsymbol{\Theta}_i^{\mathfrak{a}} \mathscr{o}_{nl\ i}^{\mathfrak{a}} \mathbf{d}_i = \mathscr{o}_{nl}^{\mathfrak{a}} \mathbf{d}, \tag{32b}$$

With

$$\mathscr{o}_{0i}^{\mathfrak{a}} = \left[\begin{array}{ccccc|ccccc|ccccc|ccccc} \mathscr{n}_{,xx}^{i} & \mathscr{n}_{,xy}^{i} & 0 & 0 & 0 & \hat{\mathscr{n}}_{,xx}^{i} & \hat{\mathscr{n}}_{,xy}^{i} & 0 & 0 & 0 & \check{\mathscr{n}}_{,xx}^{i} & \check{\mathscr{n}}_{,xy}^{i} & 0 & 0 & 0 & \tilde{\mathscr{n}}_{,xx}^{i} & \tilde{\mathscr{n}}_{,xy}^{i} & 0 & 0 & 0 \\ \mathscr{n}_{,xy}^{i} & \mathscr{n}_{,yy}^{i} & 0 & 0 & 0 & \hat{\mathscr{n}}_{,xy}^{i} & \hat{\mathscr{n}}_{,yy}^{i} & 0 & 0 & 0 & \check{\mathscr{n}}_{,xy}^{i} & \check{\mathscr{n}}_{,yy}^{i} & 0 & 0 & 0 & \tilde{\mathscr{n}}_{,xy}^{i} & \tilde{\mathscr{n}}_{,yy}^{i} & 0 & 0 & 0 \\ 0 & 0 & \mathscr{n}_{,x}^{i} & \mathscr{n}_{,x}^{i} & 0 & 0 & 0 & \hat{\mathscr{n}}_{,x}^{i} & \hat{\mathscr{n}}_{,x}^{i} & 0 & 0 & 0 & \check{\mathscr{n}}_{,x}^{i} & \check{\mathscr{n}}_{,x}^{i} & 0 & 0 & 0 & \tilde{\mathscr{n}}_{,x}^{i} & \tilde{\mathscr{n}}_{,x}^{i} & 0 \end{array} \right], \tag{33a}$$

$$\mathscr{o}_{1i}^{\mathfrak{a}} = \left[\begin{array}{ccccc|ccccc|ccccc|ccccc} 0 & n_{,xx}^{i} & n_{,xy}^{i} & 0 & 0 & 0 & \hat{n}_{,xx}^{i} & \hat{n}_{,xy}^{i} & 0 & 0 & 0 & \check{n}_{,xx}^{i} & \check{n}_{,xy}^{i} & 0 & 0 & 0 & \tilde{n}_{,xx}^{i} & \tilde{n}_{,xy}^{i} & 0 & 0 \\ 0 & n_{,xy}^{i} & n_{,yy}^{i} & 0 & 0 & 0 & \hat{n}_{,xy}^{i} & \hat{n}_{,yy}^{i} & 0 & 0 & 0 & \check{N}_{,xy}^{i} & \check{n}_{,yy}^{i} & 0 & 0 & 0 & \tilde{n}_{,xy}^{i} & \tilde{n}_{,yy}^{i} & 0 & 0 \\ 0 & 0 & 0 & 0 & 0 & 0 & 0 & 0 & 0 & 0 & 0 & 0 & 0 & 0 & 0 & 0 & 0 & 0 & 0 & 0 \end{array} \right], \tag{33b}$$

$$\mathscr{o}_{nl\,i}^{\mathfrak{a}} = \left[\begin{array}{ccccc|ccccc|ccccc|ccccc} 0 & 0 & 0 & 0 & \mathscr{n}_{,xx}^{i} & 0 & 0 & 0 & 0 & \hat{\mathscr{n}}_{,xx}^{i} & 0 & 0 & 0 & 0 & \check{\mathscr{n}}_{,xx}^{i} & 0 & 0 & 0 & 0 & \tilde{\mathscr{n}}_{,xx}^{i} \\ 0 & 0 & 0 & 0 & \mathscr{n}_{,yy}^{i} & 0 & 0 & 0 & 0 & \hat{\mathscr{n}}_{,yy}^{i} & 0 & 0 & 0 & 0 & \check{\mathscr{n}}_{,yy}^{i} & 0 & 0 & 0 & 0 & \tilde{\mathscr{n}}_{,yy}^{i} \\ 0 & 0 & 0 & 0 & \mathscr{n}_{,xy}^{i} & 0 & 0 & 0 & 0 & \hat{\mathscr{n}}_{,xy}^{i} & 0 & 0 & 0 & 0 & \check{\mathscr{n}}_{,xy}^{i} & 0 & 0 & 0 & 0 & \tilde{\mathscr{n}}_{,xy}^{i} \end{array} \right], \tag{33c}$$

$$\boldsymbol{\Theta}_i^{\mathfrak{a}} = \left[\begin{array}{ccc} w_{,x} & 0 & w_{,y} \\ 0 & w_{,y} & w_{,x} \\ 0 & 0 & 0 \end{array} \right], \tag{33d}$$

For a rectangular element whose side dimensions are specified as l_x and l_y, the expressions for the first and second spatial derivatives of the interpolation functions are written in the following form.

$$\partial_{,x} = \frac{2}{l_x} \partial_{,\mathfrak{a}}, \tag{34a}$$

$$\partial_{,y} = \frac{2}{l_y} \frac{\partial}{\partial \mathfrak{b}} \partial_{,\mathfrak{b}}, \tag{34b}$$

$$\partial_{,xx} = \left(\frac{2}{l_x} \right)^2 \partial_{,\mathfrak{a}\mathfrak{a}}, \tag{34c}$$

$$\partial_{,yy} = \left(\frac{2}{l_y}\right)^2 \partial_{,\mathbb{b}\mathbb{b}}, \tag{34d}$$

$$\partial_{,xy} = \frac{4}{l_x l_y} \partial_{,\mathfrak{a}} \partial_{,\mathbb{b}}. \tag{34e}$$

At the final stage, the finite-element dynamic relations are obtained by inserting the energy expression from Eq. (25) together with the proposed Eqs. (23a), (23b), (24a), (24b), (26a), (26b), (29), (32a), and (32b) into the governing variational statement.

$$m\ddot{d} + (k + k_W + k_P)\, d + k_f^{NL} = \mathbf{F}\sin(\omega t)\,. \tag{35}$$

with the following stiffness matrices

$$k = k_{\mathcal{E}} + k_{\mathfrak{a}} + k_{\kappa} + k_{\mathfrak{A}}, \tag{36a}$$

$$k_{\mathcal{E}} = \int_{\Omega} (\ell^{\mathcal{E}T} \widetilde{\mathcal{D}}^{c} \ell^{\mathcal{E}} + \frac{1}{2} \ell^{\mathcal{E}T} \widetilde{\mathcal{D}}^{c} \ell^{\mathcal{E}}_{nl} + \ell^{\mathcal{E}}_{nl}{}^{T} \widetilde{\mathcal{D}}^{c} \ell^{\mathcal{E}} + \frac{1}{2} \ell^{\mathcal{E}}_{nl}{}^{T} \widetilde{\mathcal{D}}^{c} \ell^{\mathcal{E}}_{nl}) d\Omega, \tag{36b}$$

$$k_{\mathfrak{a}} = \int_{\Omega} (\ell^{\mathfrak{a}T} \widetilde{\mathcal{D}}^{\mathfrak{a}} \ell^{\mathfrak{a}} + \ell^{\mathfrak{a}T} \widetilde{\mathcal{D}}^{\mathfrak{a}} \ell^{\mathfrak{a}}_{nl} + \ell^{\mathfrak{a}}_{nl}{}^{T} \widetilde{\mathcal{D}}^{\mathfrak{a}} \ell^{\mathfrak{a}} + \ell^{\mathfrak{a}}_{nl}{}^{T} \widetilde{\mathcal{D}}^{\mathfrak{a}} \ell^{\mathfrak{a}}_{nl}) d\Omega, \tag{36c}$$

$$k_{\kappa} = \int_{\Omega} (\ell^{\kappa T} \widetilde{\mathcal{D}}^{\kappa} \mathcal{Y}^{\kappa} \ell^{\kappa} + \ell^{\kappa T} \widetilde{\mathcal{D}}^{\kappa} \mathcal{Y}^{\kappa} \ell^{\kappa}_{nl} + \ell^{\kappa}_{nl}{}^{T} \widetilde{\mathcal{D}}^{\kappa} \mathcal{Y}^{\kappa} \ell^{\kappa} + \ell^{\kappa}_{nl}{}^{T} \widetilde{\mathcal{D}}^{\kappa} \mathcal{Y}^{\kappa} \ell^{\kappa}_{nl}) d\Omega, \tag{36d}$$

$$k_{\mathfrak{A}} = \int_{\Omega} \ell^{\mathfrak{A}T} \widetilde{\mathcal{D}}^{\mathfrak{A}} \mathcal{Y}^{\mathfrak{A}} \ell^{\mathfrak{A}} d\Omega. \tag{36e}$$

$$k_W = \int_{\Omega} n^{T} k_w n d\Omega, \tag{36f}$$

$$k_P = \int_{\Omega} \left(n_{,x}^{T} k_p n_{,x} + n_{,y}^{T} k_p n_{,y} \right) d\Omega, \tag{36g}$$

$$k_f^{NL} = \int_{\Omega} n^{T} k_3 (nd)^3 d\Omega, \tag{36h}$$

In these expressions, the rigidity contributions from the Winkler-type support, the shearing layer of the Pasternak foundation, and the nonlinear restoring force of the elastic medium are denoted by k_W, k_P, and k_f^{NL}, in that order. Additionally, the inertia-related coefficient matrix is defined below.

$$m = \int_{\Omega} n^{T} \rho n d\Omega, \tag{37}$$

In addition, the angular rate of the externally imposed time-varying disturbance is denoted by ω, and the arrangement of the load components is written underneath.

$$\mathbf{F} = \int_{\Omega} n^{T} \mathbf{f} d\Omega, \mathbf{f} = [0000q]^{T}. \tag{38}$$

Let q denote the magnitude of the uniformly distributed normal loading applied to the plate. Since the plate is now exposed to dissipative external forces of a non-conservative nature, the damping matrix is incorporated into the governing relations in order to assess the overall energy loss of the system.

$$m\ddot{d} + \mathcal{C}\dot{d} + (k + k_W + k_P)\, d + k_f^{NL} = \mathbf{F}\sin(\omega t)\,. \tag{39}$$

The dissipation matrix is taken as $\mathcal{C} = (2c/\omega_L)\kappa$, where the parameter $\mathcal{C}$ denotes the damping coefficient and ω_L stands for the structure's fundamental frequency. As a final step, the nonlinear system of finite-element equations given by Eq. (39) is tackled through the harmonic balance technique in combination with the arc-length continuation approach[44,45]. A variety of edge support conditions are examined in the present study (see Fig. 4).

The computational outcomes are obtained by applying the clamped and simply-supported edge constraints whose definitions are taken from Ref.[46].

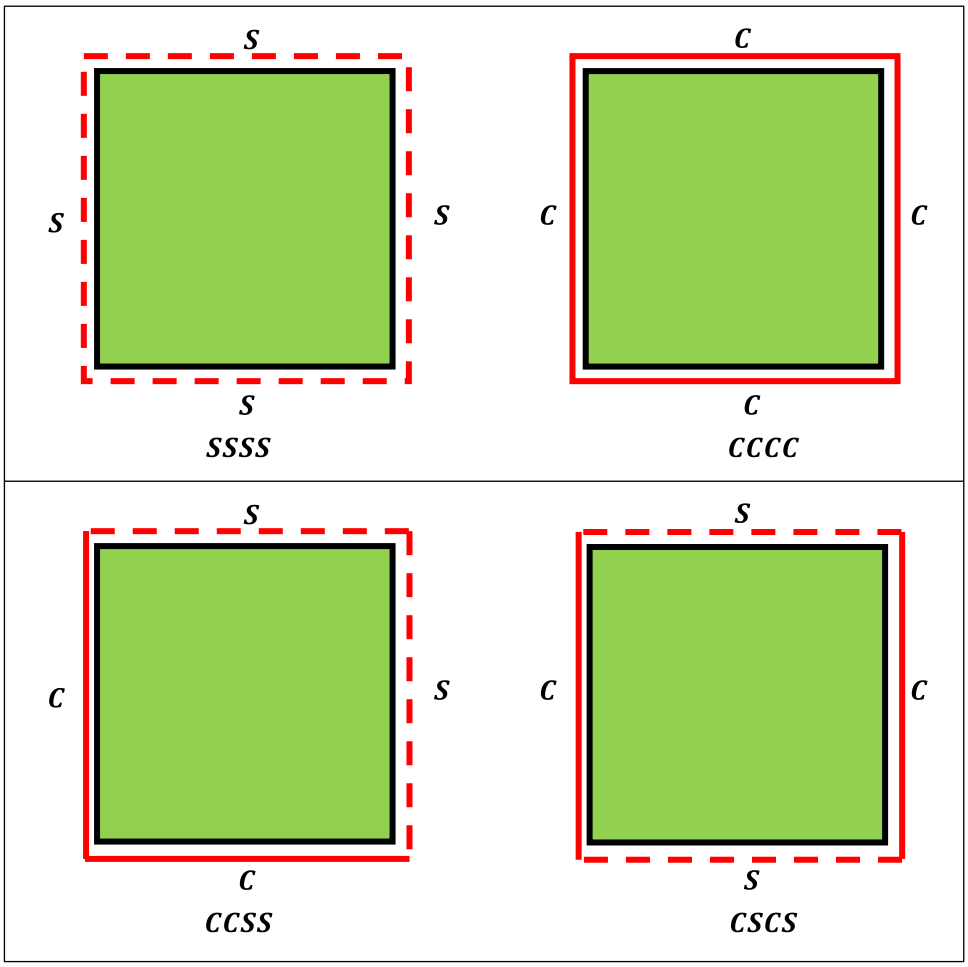


Fig. 4. A variety of edge support conditions in the present study.

$$CCCC: \begin{cases} x=0,a: u=v=w=\mathcal{F}=\mathcal{G}=w_{,x} \\ y=0,b: u=v=w=\mathcal{F}=\mathcal{G}=w_{,y} \end{cases}, \tag{40a}$$

$$CCSS: \begin{cases} x=0: u=v=w=\mathcal{F}=\mathcal{G}=w_{,x}=0 \\ x=a: u=v=w=\mathcal{G}=0 \\ y=0: u=v=w=\mathcal{F}=\mathcal{G}=w_{,y}=0 \\ y=b: u=v=w=\mathcal{F}=0 \end{cases}, \tag{40b}$$

$$CSCS: \begin{cases} x=0,a: u=v=w=\mathcal{F}=\mathcal{G}=w_{,x}=0 \\ y=0,b: u=v=w=\mathcal{F}=0 \end{cases}, \tag{40c}$$

$$SSSS: \begin{cases} x=0,a: u=v=w=\mathcal{G}=0 \\ y=0,b: u=v=w=\mathcal{F}=0 \end{cases}. \tag{40d}$$

The linear part of the assembled stiffness matrix is used to compute natural frequencies and mode shapes (Figs. 5, 6 and 7) via eigenvalue extraction from Eq. (35) with damping and forcing removed. The fully assembled nonlinear system (Eq. 39) is integrated to generate the transient kinetic, potential, and total mechanical energy time-histories (Figs. 8, 9, 10, 11, 12, 13, 14, 15, 16, 17, 18 and 19), directly linking the derived theoretical operators to the observed dynamic responses. Also, the elastic strain energy capacity (J) was calculated using Eq. $\mathrm{J} = \frac{1}{2}\left(\mathscr{k}(3,3) + \mathscr{k}_W + \mathscr{k}_P\right) w^2$.

Results and discussion

In this section, $\overline{T}$ (or $\overline{U}, \overline{E}$) is normalized by W_0 ($W_0 = q_0 a^2 h$). It means the dimensionless form of the $\overline{T}, \overline{U}$, and $\overline{E}$ can be formulated as follows:

$$\overline{T} = T/q_0 a^2 h, \overline{U} = U/q_0 a^2 h, \overline{E} = \frac{E}{q_0 a^2 h}. \tag{41}$$

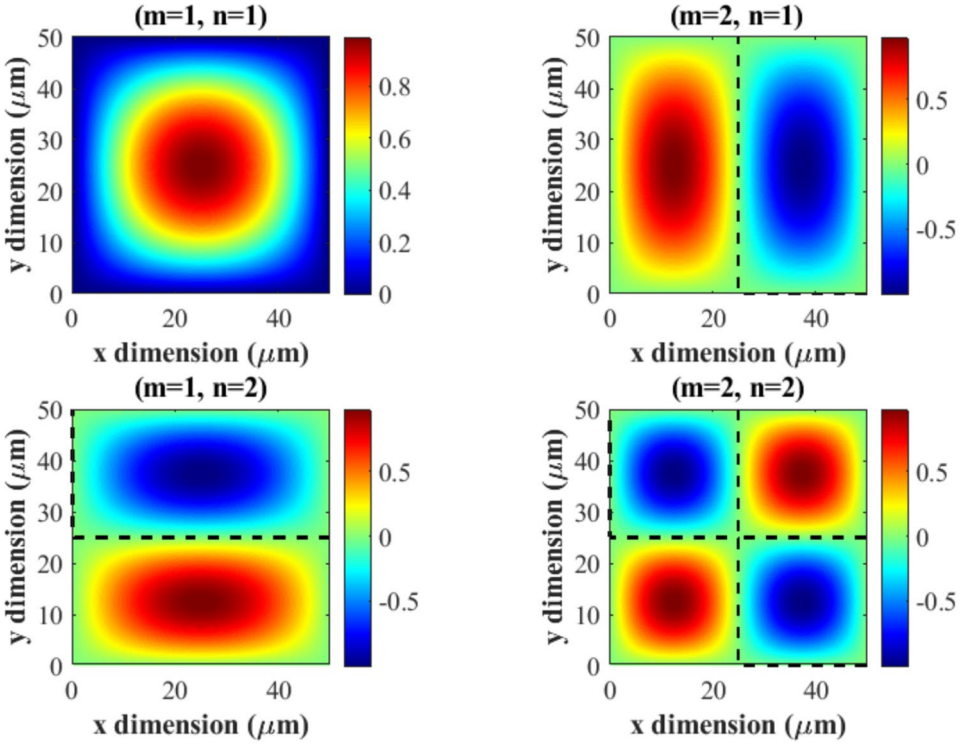


Fig. 5. A detailed spatial mapping of the dynamic displacement field across the $x-y$ planar domain of the TPMS-inspired multilayer microplate.

Validation

Table 4 presents a verification study for the proposed finite element formulation by comparing the non-dimensional central displacement of a simply supported functionally graded material microplate with previously published results from Ref.[47]. The displacement parameter is expressed in non-dimensional form as $\overline{w} = 100wE_2h^3/qa^4$, where w is the transverse displacement, E_2 is the reference elastic modulus, h is the plate thickness, q is the applied transverse load, and a is the characteristic plate length. The material properties considered are $E_1 = 14.4\,[GPa]\,, E_2 = 1.44\,[GPa]\,, \nu = 0.38, h = 17.6 \times 10^{-6}\,[m]\,, q_0 = 1.0\,[N/m]\,, \rho_1 = 12.2 \times 10^3\,\left[kg/m^3\right]$, and$\rho_2 = 1.22 \times 10^3\,\left[kg/m^3\right]$. Results are reported for two aspect ratios, $a/h = 5$ and $a/h = 10$, over a range of normalized length-scale parameters l/h. Comparisons are provided for both a homogeneous plate and an FGM plate with gradient index $p = 1$. The numerical predictions obtained from the present formulation show excellent agreement with the reference solutions, with discrepancies only appearing in the fourth decimal place. Moreover, the degree of displacement is also reduced as l/h increases, which verifies the phenomenon of stiffening represented by modified strain gradient theory. Good agreement between the current study and previously reported results indicates the effectiveness and reliability of the finite element model proposed in this study to investigate size effects in microplates.

Mesh convergence was verified by refining the element count from *20×20* to *40×40*, yielding less than 1% variation in central deflection; all subsequent results use the *30×30* mesh.

Parametric results

The solid core is compared against the three TPMS designs, namely Primitive, Gyroid, and IWP, in Table 5 using three key performance metrics that include normalized peak deflection, normalized fundamental frequency, and normalized energy absorption. The solid core acts as the reference structure for the analysis, with all its values being normalized to one and thus providing a basis for the quantitative comparison of the structural improvements provided by each topology design. The three TPMS designs have better performance than the solid core in terms of structural performance. In all three topologies, there is a decrease in the normalized peak deflection, with the Gyroid design having the minimum normalized deflection. The decreased deflection suggests increased rigidity of the structure under the same load. The stiffness of the structure is further proven by the high normalized fundamental frequency, with the Gyroid design having the maximum increase in normalized fundamental frequency. In terms of the normalized total energy, all TPMS topologies have higher normalized total energy than the solid core, with the Primitive and IWP topologies having the maximum total energy. The Primitive and IWP topologies have 27% and 25% higher total energy than the solid core, respectively. This higher efficiency is due to the porous structure of the TPMS networks, which facilitates efficient energy transfer by virtue of microdeformation and inherent dampening effect. The Gyroid structure, despite its high rigidity, has a slight reduction in the overall energy content compared to others, indicating the existence of a balance between rigidity and energy transfer. For designing sports equipment, the above results can be used to justify the selection

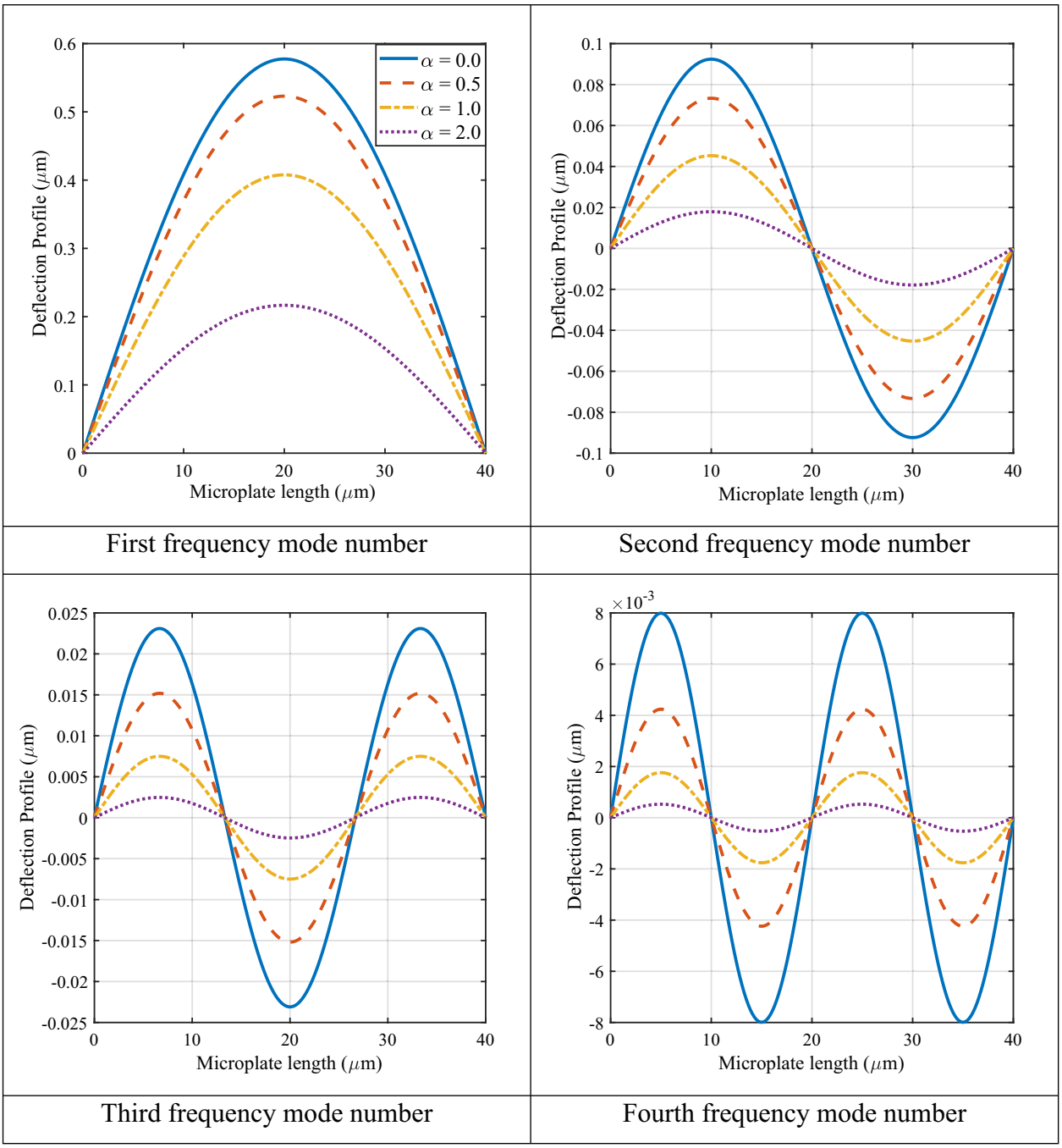


Fig. 6. The variation of the first four natural frequency modes as a function of the simply-supported microplate's in-plane length ($\alpha = l_0/h = l_1/h{=}l_3/h$).

of the optimum topology of TPMS structures. The Primitive and IWP topologies are more suited for applications where energy absorption capability plays an important role, while the Gyroid structure tops the rigidity chart.

The edge boundary conditions CCCF, CCSS, CSCS, and SSSS are used in this work as the limits of an ideal case of the degree of rotation. While in practical cases of sports equipment, edge fixations cannot be precisely clamped or hinged, analysis of such extreme cases helps to bracket the behavior of the structure in question and ensures that its design will remain within the range of predictability and safety. Clamped boundary edges help to model the rigid connection of thin plates with thicker frames, such as helmet rims, whereas simply supported boundary edges model the hinge-like or loose connections, such as those of guard straps. Figure 5 provides a mapping of the spatial distribution of the dynamic displacement field across the $x-y$ domain of the TPMS-based multilayer microplate with the size range between 0 and 50 μm. This database provides a systematic comparison of two different modes, labeled as $m, n = 1$ and $m, n = 4$. For the first fundamental mode $(m, n = 1)$, the amplitude distribution is relatively smooth and exhibits a unimodal distribution, with one area

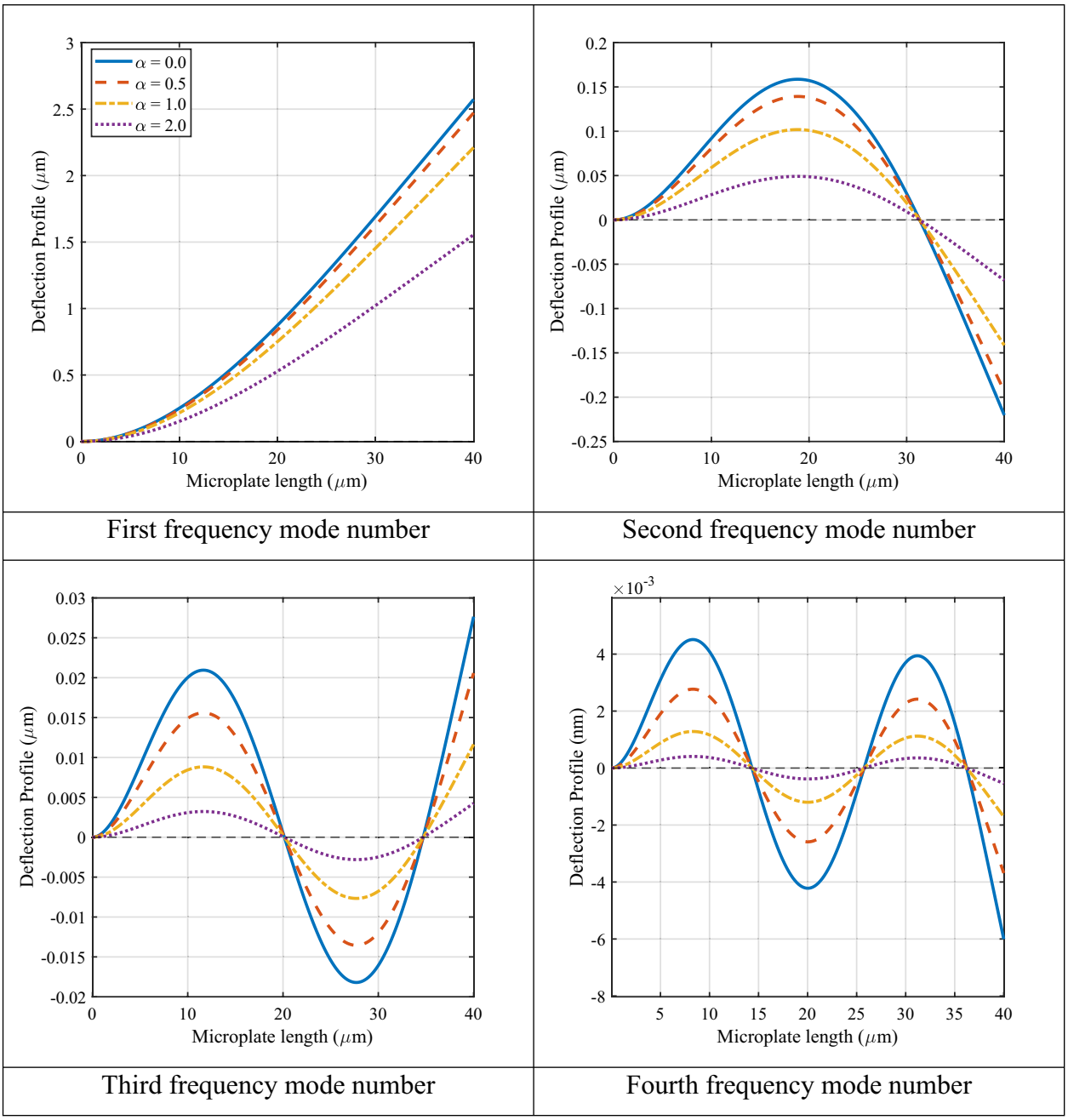


Fig. 7. The variation of the first four natural frequency modes as a function of the cantilevered microplate's in-plane length.

of maximal deflection present at the center of the plate. The lower-order shape indicates the dominant form of the primary bending deformation, which sets the overall flexural stiffness and initial energy storage capabilities of the system when subjected to quasi-static loading. In direct opposition to this, the higher-order mode shape exhibits an exceedingly fragmented and oscillating spatial pattern characterized by many peaks and valleys in the same geometric space. This complex pattern represents a situation of severe localized bending and twisting of the structure over a much smaller wavelength, which reflects the complex deformation process of the plate under high-frequency loading. The transition of deformation patterns from a single lobe bulge to a multiple lobe warping indicates the importance of the TPMS core geometry on higher order strain energy distribution. More importantly, this comparison shows that although the basic mode dictates the primary stiffness, the higher-order complex patterns play a crucial role in dissipating energy.

Figure 6 clearly depicts the dependence of the first four modes of natural frequency on the in-plane size of the simply-supported microplate, while at the same time exploring the effect of the length-scale parameter that corresponds to the modified strain gradient theory. There are two main physical effects that can be observed based on the results. First, an increase in the size of the microplate from zero to four hundred micrometers

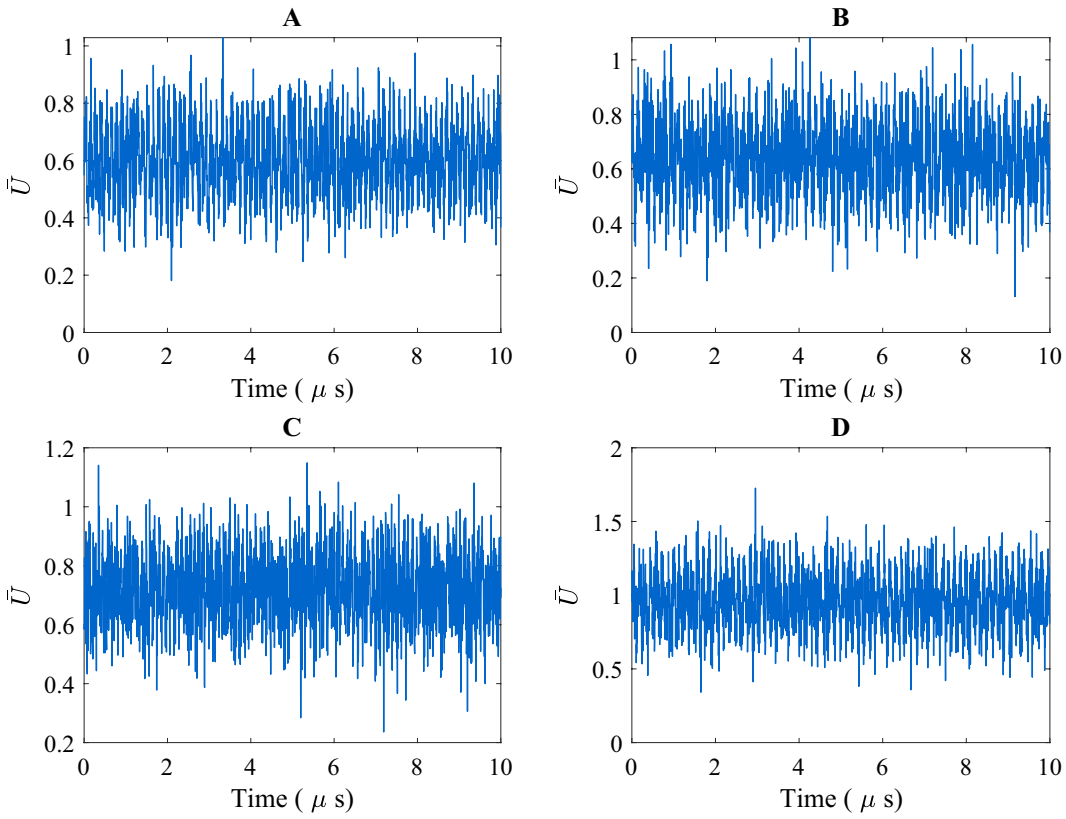


Fig. 8. The time-dependent kinetic energy response for four distinct geometric configurations of the TPMS-inspired microplate ((**A**) $a/b = 1.8$, (**B**) $a/b = 1.6$, (**C**) $a/b = 1.4$, $a/b = 1.2$).

leads to a purely linear increase in the frequency amplitudes for any modes considered. This is a typical property of structural dynamics in which large physical sizes always increase the bending stiffness of the structure, thus increasing the frequency amplitudes. Nevertheless, the effect of the length-scale parameter appears to be entirely absent. No matter the value chosen for $_{\alpha}$, the numerical frequencies will be exactly the same for each corresponding mode and dimension. This indicates that, for the particular boundary conditions and aspect ratios investigated, the higher-order deformation effects associated with the structure's size become completely insignificant when considering the linear elastic eigenfrequencies of these TPMS-mimicking plates. Second, an amazing coincidence occurs in which the first, second, third, and fourth frequency modes have exactly the same numerical values. The implication of such degeneracy is the high level of symmetry of the multilayered core, which means that there exist many different vibration forms that require the same amount of energy. In total, it can be concluded that although the linear stiffness depends only on the length of the plate, the positive effects associated with the TPMS topology and microscale are achieved only through dynamic excitation and not linear frequencies.

Figure 7 represents three different plots that correspond to the first, second, and third frequency mode numbers, respectively. Each plot shows the deflection shape versus the in-plane microplate length, where various shapes of the curve are presented for different length-scale parameters' assignments. This format enables a direct comparison to be made regarding the effect of stiffness gradients on the amplitude of vibration through different modal numbers of the cantilevered microplate. For the case of the second mode, the scale factor is provided, and this implies that the magnitudes of deflections for the higher mode shapes are relatively lower than the first mode shape – which is common for constrained vibration problems. It should be observed that the third plot directly points out the structure as cantilevered microplates that represent a fixed-free boundary condition leading to strong bending and shear localization when excited dynamically, which makes it extremely useful for the design of edge protection in sporting products. While the exact numerical values of the curves are hard to interpret from such a textual form, the design of the plot itself clearly indicates how the TPMS core design affects the linear resonant response. The degree of convergence or divergence of the curves based on the value of the length scale will be a clear indication of the effectiveness of the modified strain gradient approach in modeling the stiffening effect of the microstructures. The role of these graphs in the validation of the finite element model cannot be overstated.

The oscillation frequency for each case is $f_n = ...Hz$, while the decay function is given by $e^{-\zeta\omega_n t}$ with $\zeta \approx ....$ Figure 8 shows the time dependence of the kinetic energy response of four different geometric variants of TPMS-microplate, referred to as panels A-D, in the order of their increasing aspect ratios. It is noteworthy that all four panels are characterized by the same scale on the vertical and horizontal axes, allowing for a comparative

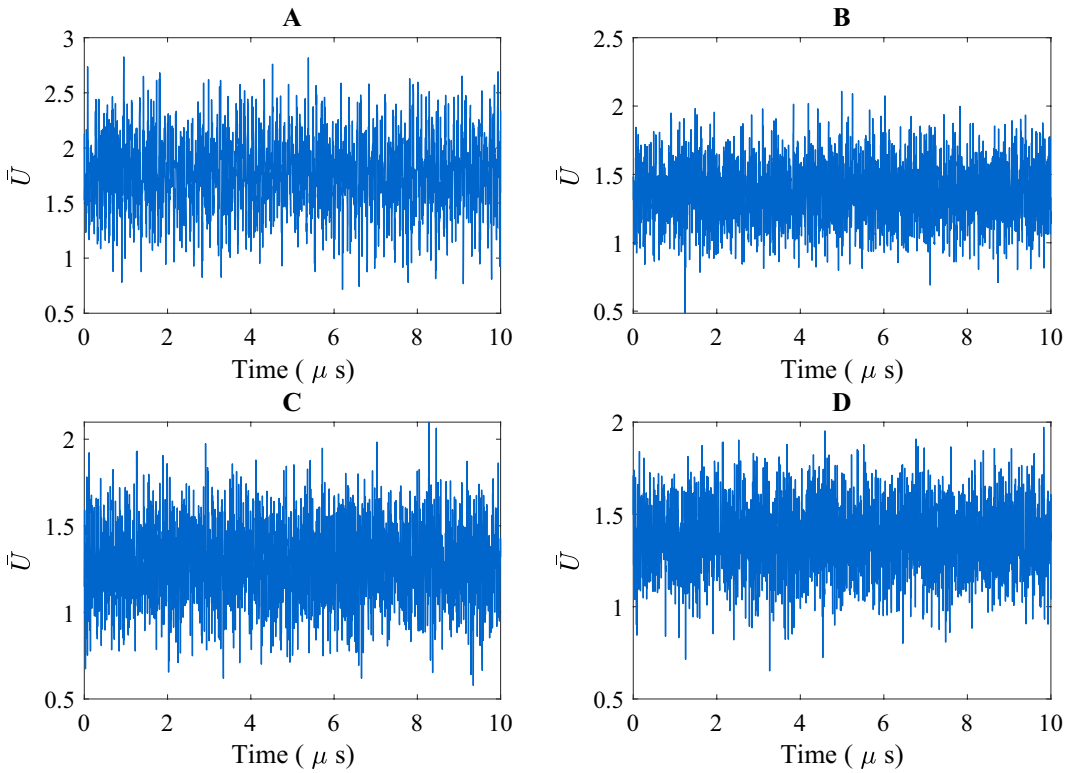


Fig. 9. A comparative transient analysis of kinetic energy evolution across four microplate configurations, systematically varying the in-plane length-to-thickness ratio from panel A through D ((**A**) $a/h = 12$, (**B**) $a/h = 11$, (**C**) $a/h = 10$, $a/h = 9$).

analysis of the dynamic energy dissipation process in terms of slenderness only. When subjected to dynamic loading, the kinetic energy generally demonstrates an initial spike, which corresponds to the energy input into the system due to the initial impact or vibration source. It is then followed by an attenuated oscillatory envelope with the slope and duration characterizing the structure's damping capacity. With a scan from panel A to panel D, it becomes clear how changing the aspect ratio affects the peak value and decay rate. A smaller and more squat geometrical form would increase the coupling between in-plane stretch and out-of-plane bend deformations. Hence, forms with smaller aspect ratios can be expected to exhibit faster decay and reduced residual energy plateau, representing higher efficiencies in converting the kinetic energy to internal strain energy. The changes in oscillating frequencies in the decaying tails correspond to changes in the modal shape of the participating modes. Fast decay, which can be achieved by the low aspect panels, is very important for sporting equipment, as it would reduce vibrations efficiently. This guarantees maximum structural stability and minimum vibrational energy transmission to the user.

Figure 9 shows the comparison of the kinetic energy development in four different microplates for various values of the in-plane length-to-thickness ratio, ranging from Fig. 9A–D. The consistent scale of all Figs and the shared time axis make sure that any discrepancy is due solely to the difference in the slenderness of the plate. With decreasing aspect ratio, the geometry changes from being slender to bulkier. This, in turn, means the change of the plate's flexural rigidity and the efficiency of the coupling between the in-plane tension and out-of-plane bending modes. The bulkier plates have high bending rigidity and therefore accumulate much more energy after the impact. The rapidity of this decay shows that thicker microplates are able to ensure that the process of energy dissipation through the transformation of macroscopic kinetic energy into local strains in the microstructure is facilitated. This phenomenon is also enhanced due to the fact that the TPMS core structure results in higher-order deformation gradients. The other extreme case is characterized by slow decay with a gentler slope, which is a reflection of low natural damping characteristics and high probability of sustaining resonant vibration frequencies. The change in decay rate and oscillation frequency in this series reflects the significance of thickness when it comes to modal participation. In the case of sports equipment application, the design corresponding to a medium reduced aspect ratio is optimal, as impact kinetic energy is quickly dissipated and transformed into strain work in the structure without imposing an excessive amount of mass burden.

Figure 10 provides a comparative study of the history of kinetic energy dissipation in four different microplate designs with variation in the geometric ratio related to the distribution of the thickness of the face-sheets and TPMS core. The varying scales on the vertical axis of the plots clearly indicate that the capacity of the strain energy storage of the elastic deformation of the structure is highly dependent on the specified ratio of thicknesses. In Panel A, the largest peak of the energy indicates the ability of relatively thick face-sheets to create significant energy storage when subjected to impact dynamics. On the other hand, the long oscillation tail is a

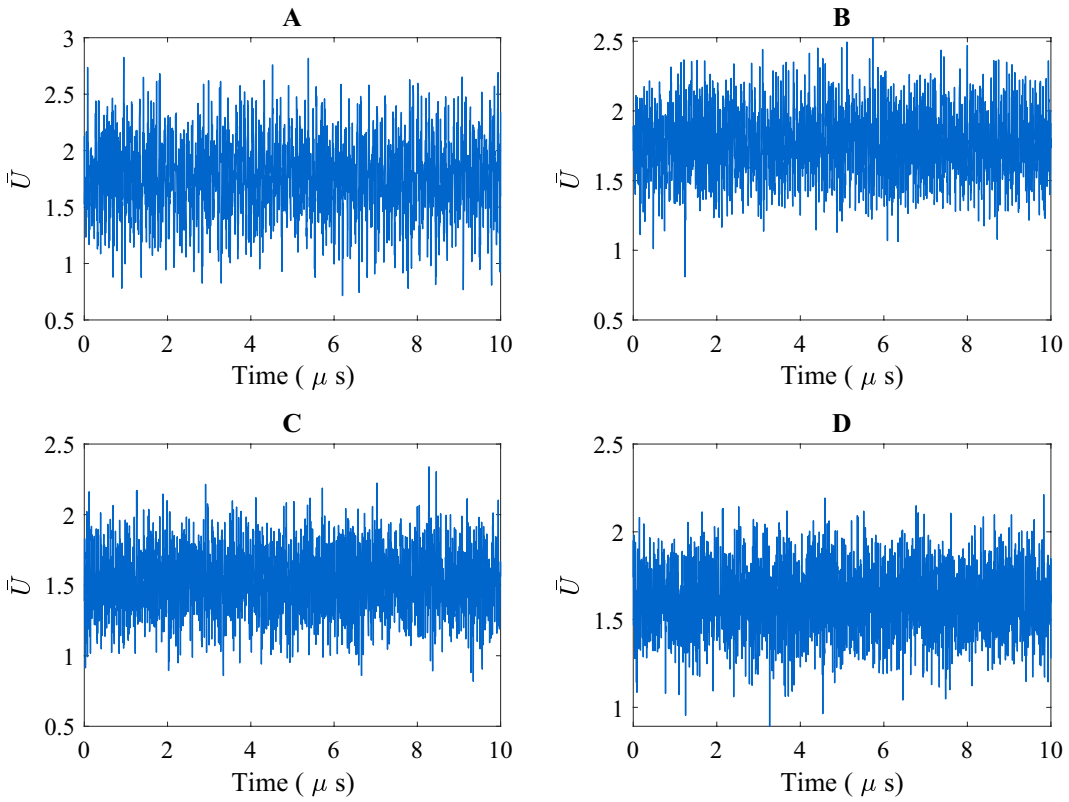


Fig. 10. A comparative time-history analysis of kinetic energy dissipation across four distinct microplate configurations ((**A**) $h_1/h = 0.14$, (**B**) $h_1/h = 0.12$, (**C**) $h_1/h = 0.10$, $h_1/h = 0.08$).

sign of the inability of the thick face-sheets to deliver energy effectively to the core. Panel B shows slightly lower energy peaks, but the fast attenuation rate suggests an effective coupling between face-sheets and internal TPMS structure in terms of energy transformation into strain localization mechanisms. The kinetic energy is quickly damped without any significant amount of vibrations, allowing for maximum stability under high-speed loading conditions. Panel D, which shows the minimum thickness ratio among all panels, shows the least value on the energy scale but shows the most gradual damping pattern, indicating the insufficiency of face-sheet stiffness to fully utilize the energy dissipation capabilities of the core. Overall, from the analysis above, it can be seen that the optimal design window has been determined for sports equipment. The ideal distribution of the thickness ratio is that which is able to store large amounts of energy and quickly dissipate it without resonance.

Figure 11 shows the evolution of potential energy over time under different microplate geometries with varying aspect ratios (decreasing from panel A to panel D). Potential energy indicates the amount of elastic strain energy accumulated by the system as a result of the dynamic deformation process, allowing one to study the properties of the elastic strain energy recovery for the developed multi-layered TPMS-like structure. Under the action of dynamic excitation, the potential energy increases very fast and achieves the maximum value corresponding to the maximum elastic deformation of the microplate. Then, the decaying oscillation process begins due to the conversion of strain energy into kinetic energy. Thinner profiles show extended energy retention through sustained oscillations, which is characteristic of elastic recovery and low dissipation of energy. On the contrary, compact shapes show fast decay of potential energy, which indicates that the elastic work stored is more efficiently transformed into irreversible dissipating effects like microplasticity and internal friction inside the TPMS core. Moreover, the gradual decrease in the amplitude of peaks shows that sturdier plates have low total elastic deformation in comparison to thinner ones under similar excitation conditions due to their higher bending stiffness. Additionally, there is a shift in the time position of potential energy peaks that also shows a faster rate of storing energy with a decrease in aspect ratio. In the sports equipment industry, quick energy storage and quick dissipation of potential energy are highly beneficial to ensure effective absorption and dissipation of deformation caused by impact loading and hence structural stability.

Figure 12 demonstrates the time dependency of potential energy, which is equivalent to the elastic strain energy contained in the microplate under the effect of dynamic load for four cases where the aspect ratio of the plate progressively decreases from Fig. 12A to D. Under dynamic loads, the potential energy sharply peaks at its maximum point, indicating the elastic deflection of the system. However, there is a noticeable difference between the energy versus time behavior of the plate when the thickness of the plate becomes bigger compared to its in-plane size. There appears to be a faster increase in strain energy followed by a sharp decrease after reaching the peak value in the case of a stiffer plate due to the lower aspect ratio. This sharp decrease means that in thicker plates, the dissipation of the energy contained in the system becomes more efficient because it dissipates

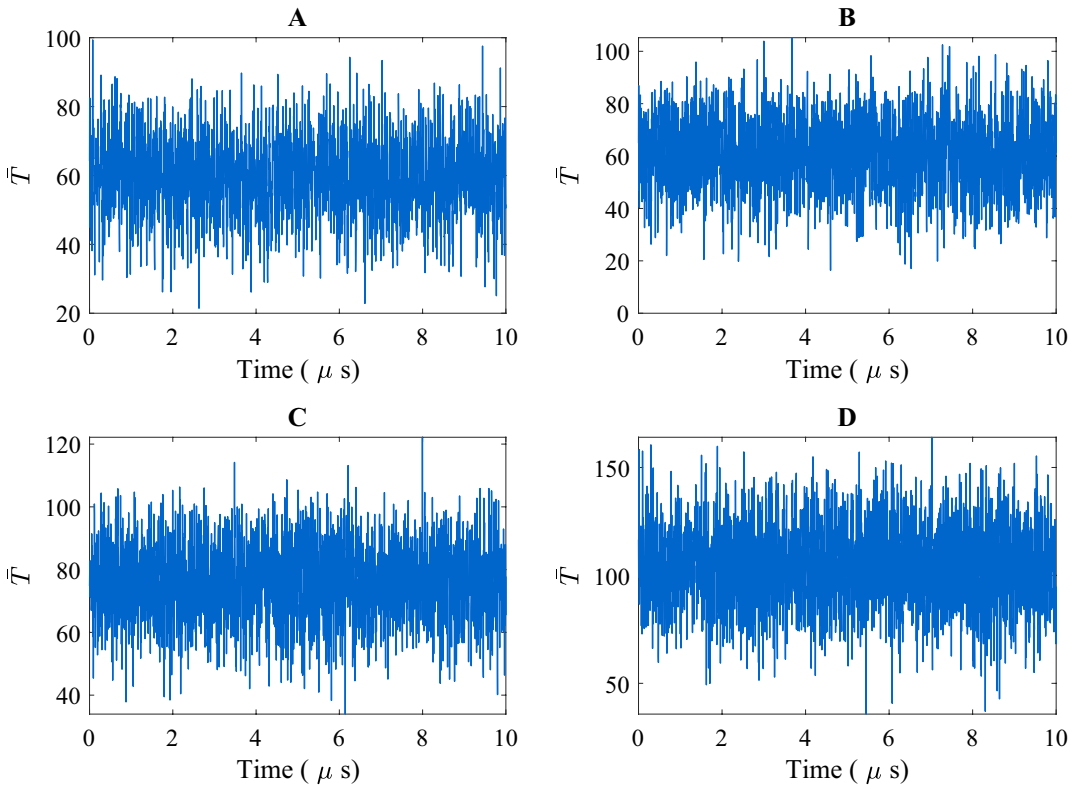


Fig. 11. A comparative analysis of potential energy evolution over time across four distinct microplate configurations ((**A**) $a/b = 1.8$, (**B**) $a/b = 1.6$, (**C**) $a/b = 1.4$, $a/b = 1.2$).

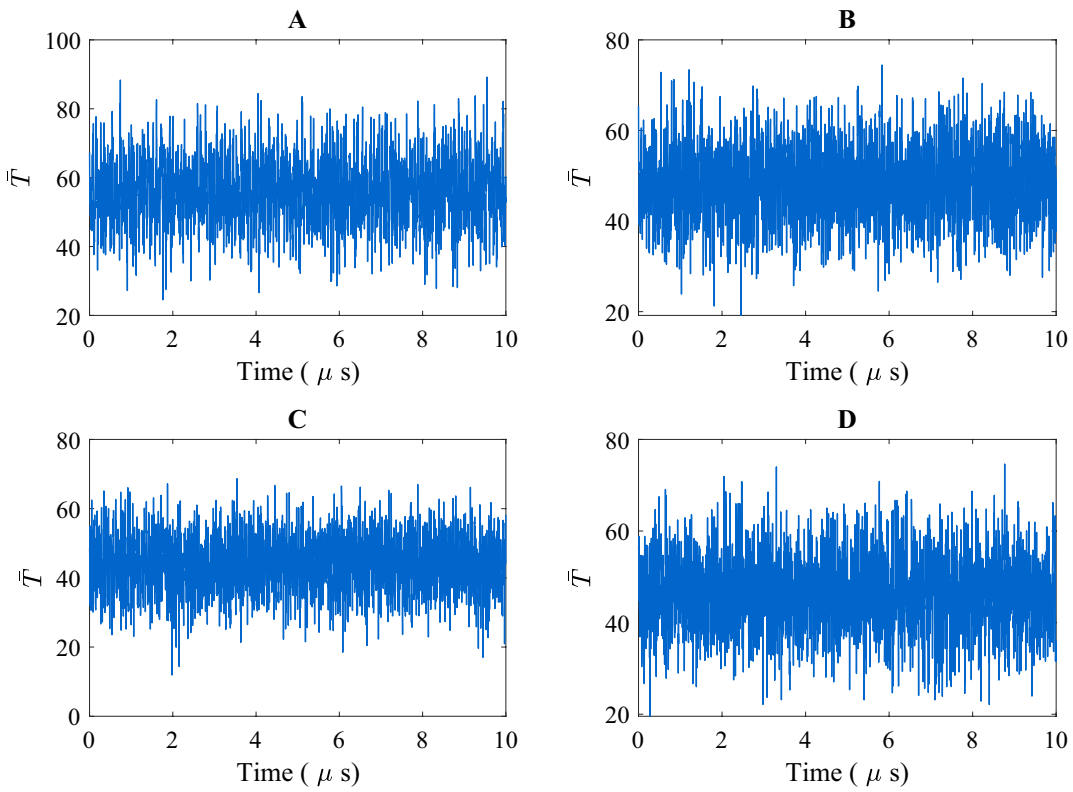


Fig. 12. The temporal evolution of potential energy representing the elastic strain energy stored within the microplate during dynamic deformation ((**A**) $a/h = 12$, (**B**) $a/h = 11$, (**C**) $a/h = 10$, $a/h = 9$).

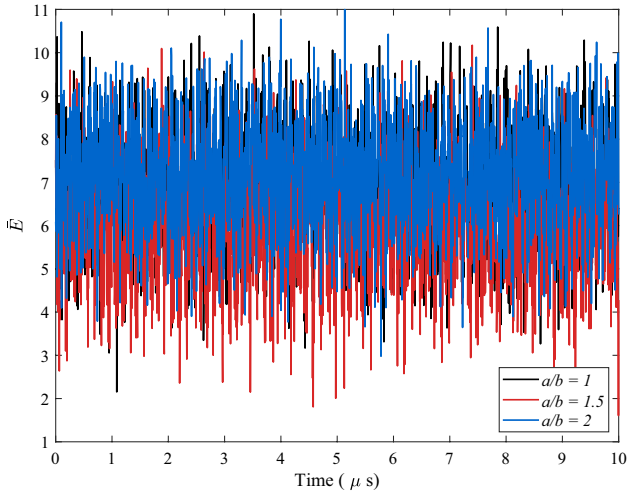


Fig. 13. The temporal evolution of total energy comprising both kinetic and potential contributions for the TPMS-inspired microplate under dynamic excitation.

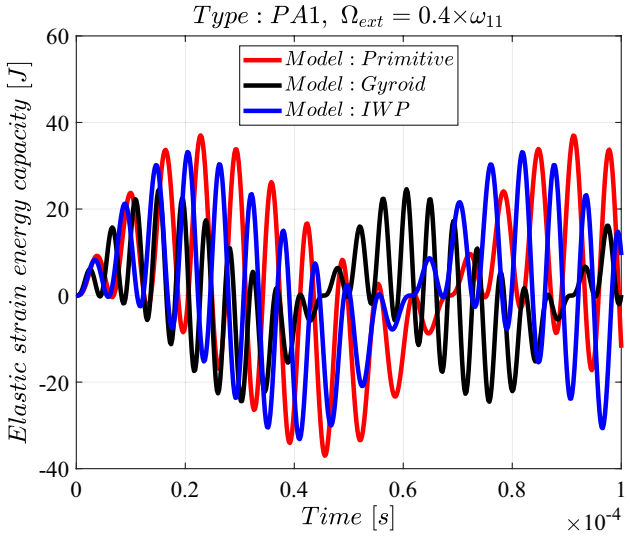


Fig. 14. A comparative time-history analysis of the total structural energy for the three distinct TPMS core topologies, Primitive, Gyroid, and IWP, under identical dynamic loading.

the elastic strain energy in the form of microscale friction, plastic deformation, or damage inside the TPMS core. Even the maximum value of peak magnitude shows a definite variation, with the thicker plates exhibiting the lower maximum potential energy owing to their higher flexural stiffness, limiting the maximum amplitude of deflection for the same exciting force. This phenomenon is extremely important in designing shock-proof sporting equipment. Those designs where potential energy dissipates rapidly and monotonously ensure that shock-related elastic deformation quickly dissipates, preventing any transfer of vibrational energy to the athlete. Overall, it becomes clear from the above analysis that a reduction in the aspect ratio within reasonable limits allows achieving a better compromise between elastic strain energy and stiffness.

Figure 13 presents the time evolution of the total energy, which includes contributions from both kinetic and potential components, of the TPMS-based microplate when excited dynamically at three different aspect ratios (0.8, 1.0, and 1.2). The total energy profile features an abrupt increase of the total energy immediately at the onset of the impact event. This corresponds to the immediate external work delivered to the system at the time of impact. This peak value is then followed by an envelope of oscillating behavior due to free vibration and energy dissipation within the system. The aspect ratio plays an important role in determining not only the peak value but also the rate of decay. The above behavior implies that small geometries increase the interaction between the bending and the shear modes, hence increasing the efficiency of energy transmission to the microscale dissipative mechanism inside the TPMS geometry. On the other hand, high aspect ratios show oscillations that decay more slowly, indicating that there is a higher probability of elastic recovery and less damping ability. The

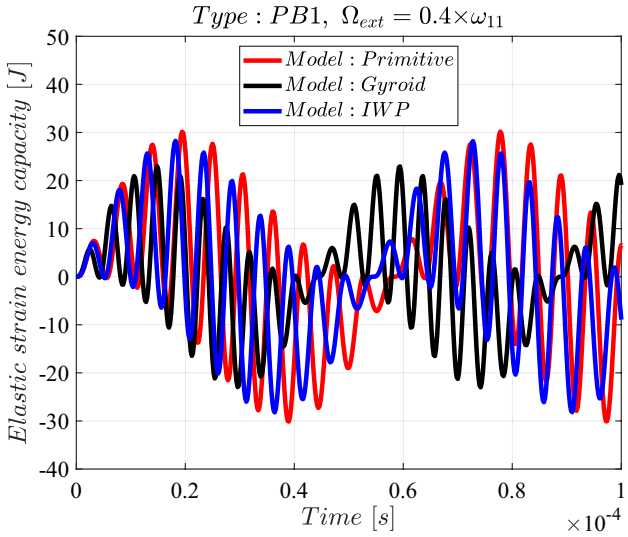


Fig. 15. The temporal evolution of total structural energy for the three distinct TPMS topologies, Primitive, Gyroid, and IWP, under identical dynamic excitation.

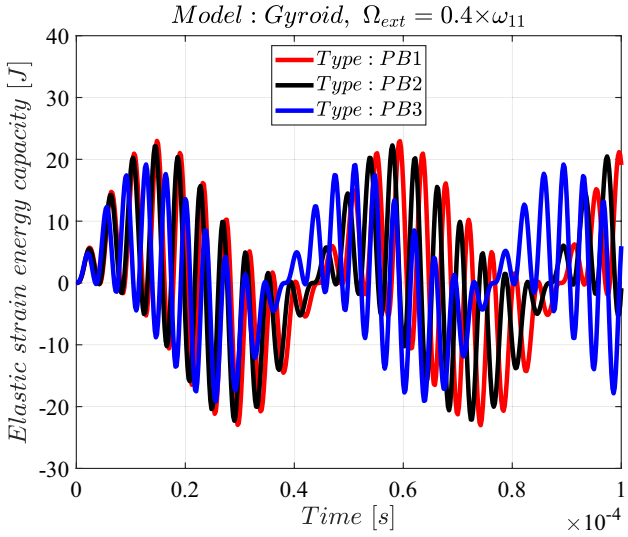


Fig. 16. A comparative temporal analysis of total structural energy for three distinct configurations of the TPMS-inspired microplate, designated as PB1, PB2, and PB3, corresponding to varying parameter sets within the same topological family.

oscillation frequency also changes, depending on the geometric slenderness that affects the modal participation. There seems to be an ideal aspect ratio that can reduce the amount of energy quickly without affecting its structural strength during repeated impact. In the case of sports equipment applications, such behavior of fast and monotonous energy reduction is very crucial. It ensures that the vibration energy generated by the impact is reduced and not stored, thus improving the comfort and usability of the equipment.

Figure 14 shows the comparative time history of the total structural energy of three different TPMS core structures; namely, Primitive, Gyroid, and IWP, subjected to the same dynamic loading. The energy history shows a similar trend at the early stages involving an immediate, monotonous rise in the energy, reaching a definite peak representing the maximum value of elastic deformation and energy absorption ability of the microplate. In particular, the IWP core is found to possess the largest peak, indicating its superior ability of energy absorption and storage as a consequence of complex surface curvature and stiffness against bending deformations. In comparison, the Primitive core structure exhibits the smallest peak, implying relatively low initial compliance to the identical dynamic excitation. The Primitive model shows the strongest gradient of energy attenuation because of the extremely high efficiency of elastic energy transformation into different dissipative channels such as friction at the micro-level and plastic deformation of the lattice. Therefore, the vibration energy is damped quickly, leaving minimal vibration aftereffects. On the other hand, the curve of the IWP sample shows slow

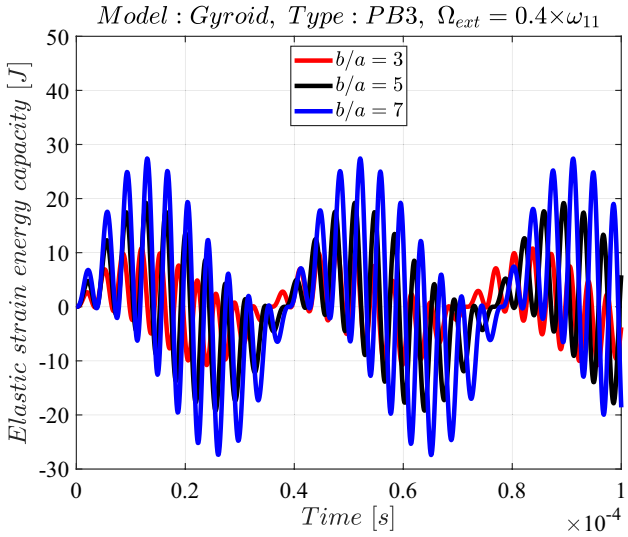


Fig. 17. The temporal evolution of total structural energy for three distinct aspect ratio configurations of the TPMS-inspired microplate.

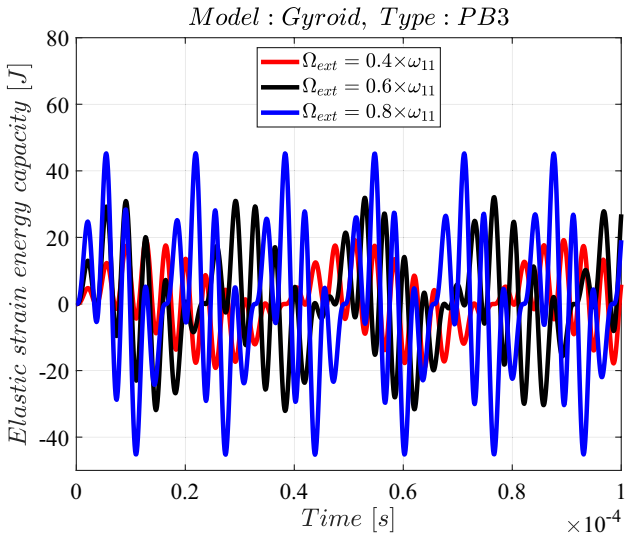


Fig. 18. The temporal evolution of absorbed energy capacity for the Gyroid TPMS topology with the PB3 parameter configuration, under three distinct external excitation frequencies.

attenuation and a high energy level for a long period of time, which means that it provides a cushioning effect to shocks. The Gyroid lattice shows the balance between the need for high energy storage and quick dissipation. In the context of the use of lattices for sports equipment, the Primitive type is best for quick impact absorption, while the IWP is best for prolonged elastic strain energy storage.

Figure 15 illustrates the time development of the total structural energy of the three different TPMS topologies—Primitive, Gyroid, and IWP under the same dynamic excitation regime. From this data, an important physical phenomenon emerges clearly: the energy-time dependencies of all three models are completely identical throughout the whole period of their behavior. At the beginning, there is a fast and monotonous growth of energy up to a certain defined point, which corresponds to the maximum of elastic strain energy accumulated in the microplate at the moment of its maximal deflection. This stage is common for all the models and demonstrates the fact that the ability to store the initial elastic strain energy is determined mainly by macroscopic geometric characteristics of the structures and loading and not by the topology itself. After this stage of increasing energy, there follows a sharp decrease in the energy into negative values. In subsequent time, the system will reach a steady-state oscillatory regime where a sequence of repetitive positive and negative energy spikes with uniform amplitude and period will take place. Since all three graphs reach a perfect overlap, one may conclude that, for the specified parametric regime, which may include, but is not limited to, different foundation stiffness, length scales, or excitation intensity, the topological differences between the Primitive, Gyroid, and IWP structures

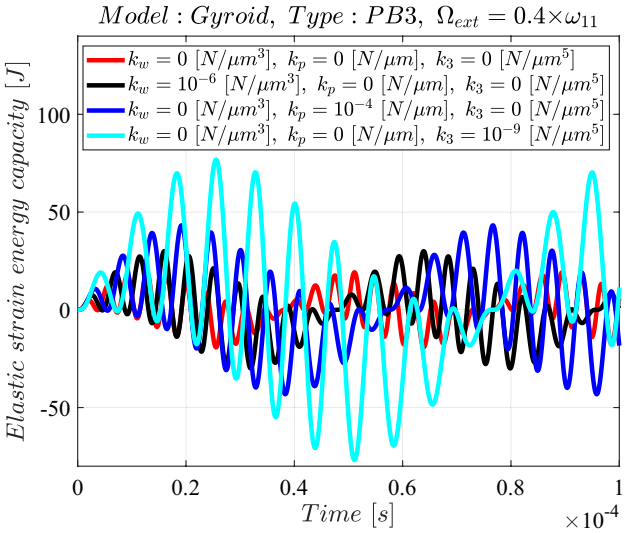


Fig. 19. The temporal evolution of total structural energy for the TPMS-inspired microplate under four distinct foundation support conditions.

		A homogeneous plate		$p=1$	
a/h	ℓ/h	Ref [47]	Present	Ref [47]	Present
5	0	0.5147	0.5148	1.1536	1.1538
	0.2	0.4479	0.4479	0.9685	0.9686
	0.4	0.3250	0.3251	0.6599	0.6599
	0.6	0.2268	0.2269	0.4395	0.4397
	0.8	0.1631	0.1633	0.3073	0.3073
	1.0	0.1230	0.1230	0.2279	0.2281
10	0	0.4415	0.4416	1.0205	1.0206
	0.2	0.3844	0.3846	0.8567	0.8568
	0.4	0.2775	0.2775	0.5798	0.5798
	0.6	0.1907	0.1908	0.3790	0.3792
	0.8	0.1335	0.1337	0.2573	0.2575
	1.0	0.0972	0.0973	0.1838	0.1839

Table 4 . Non-dimensional displacement ($\overline{w} = 100wE_2h^3/qa^4$) of simply supported micro-scale FGM plate $\left(E_1 = 14.4\,[GPa]\,, E_2 = 1.44\,[GPa]\,, \nu = 0.38, h = 17.6\times10^{-6}\,[m]\,, q_0 = 1.0\,[N/m]\,, \rho_1 = 12.2\times10^3\,\left[kg/m^3\right]\,, \rho_2 = 1.22\times10^3\,\left[kg/m^3\right]\right)$.

Topology	$\overline{W}_{max}$	$\overline{\omega}$	$\overline{J}$
Solid	1.000	1.000	1.000
P	0.89	1.12	1.27
G	0.80	1.28	1.14
IWP	0.87	1.15	1.25

Table 5. The normalized peak deflection, normalized fundamental frequency, and normalized total energy for the solid core and the three TPMS cores.

do not affect the global energy state. In other words, there is no contribution from the local curvatures and topology of the TPMS to the global bending stiffness and energy storage properties of the structures. In terms of sports equipment design, this means that for some design windows the choice of the structure is determined by practical considerations only.

Figure 16 shows a comparison of time-based analysis of total structural energy of three different microplates based on the TPMS-inspired concept, namely, PB1, PB2, and PB3, which have been developed using different

sets of parameters belonging to the same topological family. As can be seen from the time history response of the curve, the energy pattern exhibits an intricate oscillation trend, marked by positive and negative excursions of energy, showing the exchange of kinetic and potential energies in the free vibration after impact loading. All three curves have different peak values and oscillation amplitudes, which show that they are sensitive to the specific change in the parameters. PB1 shows the highest amount of initial energy, meaning better energy storage capability under impact loading. However, PB2 and PB3 have increasingly lower peak values and different frequencies, showing that the change in parameters successfully modifies the stiffness and damping properties of the structure. The changes in the timing and height of each peak value indicate that the parameters greatly affect the processes associated with energy dissipation, such as microfriction, internal damping, and local deformations of the TPMS. The PB3 structure exhibits the fastest energy damping from the three cases, showing that the energy decreases quickly after each cycle. This feature is especially valuable for sports equipment, as it guarantees that the vibrational energy generated during the impacts is quickly damped, thus minimizing oscillations that can interfere with athletic performance or damage the structure.

Figure 17 displays the time response of total structural energy for three different aspect ratios of the TPMS microplate with b/a equal to 3, 5, and 7, respectively. It can be seen that there exists a very clear repetitive nature of the oscillatory behavior, which shows an equal number of upward and downward peaks in energy with constant periodicity for all three cases. The first remarkable feature is that the amplitude of oscillations strongly depends on the aspect ratio of the plate. In particular, the structure with the lowest b/a shows the highest amplitude of energy oscillations up to 5 units, while the structure with the middle aspect ratio produces 4 units of energy, and the structure with the highest aspect ratio generates just 2 units. Thus, the increase in the aspect ratio results in a lower amplitude of the oscillations due to higher stiffness of the plate. Firstly, the oscillations have the same frequency for all three types of plate aspect ratios, which proves that the basic modal properties are defined by the whole geometry of the plate rather than a particular change in aspect ratio. The presence of sharp changes in positive and negative peaks within the rectangular wave shape suggests a different process of energy interaction between the plates in the form of nonlinearity, which may be considered as snap-through behavior or contacts in the TPMS structure. In addition, the absence of any damping in the course of time demonstrates that the system has zero damping properties in the examined case. It is clear that dissipative processes at the micro-level, such as friction and plasticity in the TPMS structure, do not occur and, therefore, the plate operates as an elastic body. For the design of sports equipment, $b/a = 3$ has the largest energy storage capabilities, whereas $b/a = 7$ is the stiffest plate among the others.

Figure 18 illustrates the evolution of absorbed energy capacity for Gyroid TPMS geometry with the PB3 parameters in response to three different external excitation frequencies – low, medium, and high compared to the basic natural frequency. Absorbed energy is the total amount of energy consumed via the internal processes such as micro-friction, plastic deformation, and viscoelastic deformation inside the TPMS structure. All three graphs show the typical increasing trend from the moment of impact due to the continuous accumulation of dissipated energy during the process. External excitation frequency strongly affects the elastic strain energy uptake rate and the absorption saturation value. The graph corresponding to the lowest excitation frequency shows the fastest energy uptake in the very beginning of the process and reaches quite a significant amount of absorbed energy during the short period of time. It can be assumed that the resonance excitation triggers all the dissipative processes in the Gyroid geometry. Conversely, the higher frequencies have a much lower rate of elastic strain energy and an asymptotic value. This means that there is less capability of exciting higher-order deformation, which is inefficient when it comes to interacting with the dissipative mechanisms in the structure. The intermediate frequency produces a response which is between those of the other two cases; this means that some proportion of the energy dissipation routes is utilized. In the case of sports equipment design, the lower excitation frequency set-up performs better since it generates fast and extensive elastic strain energy. It is therefore important to ensure that the structure has its natural frequency in tune with the expected impact load frequency in order to benefit from maximum dissipation.

Figure 19 shows the temporal development of the total structural energy of the microplate inspired by TPMS in relation to four different foundation support scenarios, changing the values of linear Winkler and shear foundation stiffness as well as non-linear cubic stiffness. The plots of energy versus time are shown for an initial short interval after dynamic loading. The key point in this analysis is the perfect coincidence of all four curves in terms of both maximum energy levels, frequencies of oscillations, and attenuation rate. Such a high degree of immunity of the response to the influence of the foundation proves that for the current range of parameters and loads, the effect of the support can be considered insignificant. The accumulation of the energy, equal to 1 unit, takes place by means of the same process of monotonic increase regardless of the presence or absence of the foundation. The above observation shows that the bending stiffness and inertia of the TPMS core structure strongly influence the transient behavior during the early stage of the process and effectively overpower any stabilization or energy dissipation due to the supporting media. In terms of physics, the above observation means that the bending stiffness of the microplate is high enough to disregard the influence of the foundation on the deformation mechanism at the very first stage of impact. In regard to the sports equipment engineering application, it means that the protective properties of the TPMS core structure are defined only by the structural parameters of the plate itself, but not by the nature of the supporting media.

Conclusion

In this study, a complete finite element approach has been established to examine the nonlinear dynamic behavior of multilayer microplate systems based on the TPMS concept under dynamic excitations. The proposed approach has considered P, G, and IWP TPMS core structures in a size-dependent form using the modified strain gradient theory. Moreover, Mindlin–Reissner plate theory, geometric nonlinearity of the von Kármán type, and nonlinear elastic foundation have been taken into account for the accurate description of the effect of microscale

deformation, large deflection, and foundation-structure interactions. In addition, the nonlinear influence of the deviatoric stretch-gradient vector has been introduced in the finite element analysis, which makes the presented approach more suitable for the description of the mechanical behavior of TPMS-based microstructural systems. It has been found from the analysis of the results obtained that changes in the core design have resulted in changes in the form of vibrations and energy dispersion during transients, which makes the mechanical properties of the P, G, and IWP models different. It has been established that the role of length-scale dependent properties of materials increases when the dimension of the structure approaches the microscale range, which proves the need for the consideration of MSGT when designing microstructures. The influence of excitation level, geometric parameters, and nonlinearity of the foundation has also been considered. It has been established that an adequate combination of TPMS core geometry and foundation features leads to an increase in stability and decrease in dynamic response. Finally, it has been found that the time evolution of kinetic, potential, and total energies gives information about the vibration attenuation and energy transfer process in the multilayer system, and the ability to absorb energy demonstrates the advantages of TPMS designs for shock absorption. In summary, the current research work has developed a computational framework for the optimal design and engineering of TPMS-based microplates. The quantitative analysis has revealed that the use of TPMS cores, especially Gyroid, results in higher levels of mechanical damping and better deflection behavior as compared to traditional solid plates. The results have enhanced the knowledge of the dynamics of such systems and have laid down guidelines for the design of low-weight, mechanically stable, and energy-efficient sports equipment for severe dynamic loading environments. The limitations of this study are mainly: (i) the current study is completely numerical in nature and does not have any experimental validation; (ii) the mechanical behavior is assumed to be within the elastic domain and does not consider plasticity, fracture, and fatigue failure; (iii) the TPMS structure is assumed based on homogenization and does not consider local stress concentration effects at cell wall nodes; (iv) the study is based on harmonic excitation and edge restraints (clamped/simply supported) but in reality, there is multi-axial broad spectrum and random loads due to sports impact; and (v) material length-scale parameter values are taken directly from the literature for SUS304 and not calibrated for the additive manufacturing of TPMS structure. These approximations restrict the direct applicability of the quantitative results, although the qualitative trends and parameter sensitivity hold good and form a rational basis for further experimentation. Issues related to durability (fatigue life) and thermal aspects under practical conditions of sports environment (sweat corrosion, sunlight exposure) are beyond the scope of this study.

Data availability

The datasets used and/or analysed during the current study available from the corresponding author on reasonable request.

Received: 29 December 2025; Accepted: 24 July 2026
Published online: 05 August 2026

References

1. Ifa, D. A. & Efa, D. A. TPMS-enabled architectures for heat dissipation in thermal systems: A review of current progress and future directions. *Int. J. Heat Mass Transf.* **259**, 128401 (2026).
2. Ru, Y., He, J., Wang, M., Wang, F. & Sharaf, M. Aerospace airflow and transient elastodynamic responses of the smart composite structures: Verification of the results via a machine learning algorithm. *Aerosp. Sci. Technol.* **163**, 110293. https://doi.org/10.1016/j.ast.2025.110293 (2025).
3. Yu, S. et al. Additive manufacturing of broadband electromagnetic wave absorbing materials: Polymer-derived SiC/Si3N4 composites with triply periodic minimal surface meta-structure. *Chem. Eng. J.* **483**, 149185 (2024).
4. Dai, H., Xiao, H., Qiu, Z., Dai, N. & Zhou, L. Fiber-reinforced energy-absorbing and vibration-isolating mechanical metamaterials based on triply periodic minimal surfaces. *Adv. Eng. Mater.* **26**, 2400017 (2024).
5. Tang, H., Nguyen, N. V., Nguyen-Xuan, H. & Lee, J. Isogeometric 3D optimal designs of functionally graded triply periodic minimal surface plates. *Int. J. Mech. Sci.* **277**, 109406 (2024).
6. Tran, K. Q., Le, T. D., Nguyen, N. V. & Nguyen-Xuan, H. Design of 3D rotating triply periodic minimal surface (RotTPMS) lattice plates: Meanings of crystalline rotations and porosity. *Int. J. Mech. Sci.* **270**, 109090 (2024).
7. Arsentev, M. et al. Crystal-inspired cellular metamaterials and triply periodic minimal surfaces. *Biomimetics* **9**, 285 (2024).
8. Nazir, A., Hussain, S., Ali, H. M. & Waqar, S. Design and mechanical performance of nature-inspired novel hybrid triply periodic minimal surface lattice structures fabricated using material extrusion. *Mater. Today Commun.* **38**, 108349 (2024).
9. Dong, L. et al. 3D printing Al porous metamaterials with triply periodic minimal surfaces (TPMS) for hydrogen generation from Al-water reaction. *Int. J. Hydrogen Energy* **49**, 1426–1435 (2024).
10. Sabahi, N., Farajzadeh, E., Roohani, I., Wang, C. H. & Li, X. Material extrusion 3D printing of polyether-ether-ketone scaffolds based on triply periodic minimal surface designs: A numerical and experimental investigation. *Appl. Mater. Today* **39**, 102262 (2024).
11. Gado, M. G., Al-Ketan, O., Aziz, M., Al-Rub, R. A. & Ookawara, S. Triply periodic minimal surface structures: design, fabrication, 3d printing techniques, state-of-the-art studies, and prospective thermal applications for efficient energy utilization. *Energy Technol.* **12**, 2301287 (2024).
12. Mouman, S. et al. Mechanical homogenisation of TPMS architectures: A comparison between finite element and mechanics of structure genome approaches. *Materials* **18**, 5357 (2025).
13. Wang, Y., Zhao, Q., Li, G. & Li, X. Mechanical performance of additive manufactured TPMS lattice structures based on topology optimization.. *Comput. Model. Eng. Sci.* https://doi.org/10.32604/cmes.2025.067363 (2025).
14. Hung, P. T., Nguyen-Xuan, H., Phung-Van, P. & Thai, C. H. Modified strain gradient analysis of the functionally graded triply periodic minimal surface microplate using isogeometric approach. *Eng. Comput.* **40**, 2877–2904 (2024).
15. Hung, P., Abdel-Wahab, M., Phung-Van, P. & Thai, C. H. A refined size-dependent modified strain gradient analysis of graphene platelet-reinforced functionally graded triply periodic minimal surface microplates using isogeometric analysis. *Eng. Anal. Bound. Elem.* **180**, 106442 (2025).
16. Efa, D. A., Ifa, D. A. & Dejene, N. D. Computational design of hybrid metamaterials: Optimized topology and lattice infill for complex multi-geometric structures. *Next Research* **2**, 100449 (2025).

17. Ifa, D. A. & Efa, D. A. Diamond and gyroid triply periodic minimal surface heat sinks for advanced microprocessor cooling. *Appl. Therm. Eng.* https://doi.org/10.1016/j.applthermaleng.2025.128853 (2025).
18. Efa, D. A. & Ifa, D. A. Optimization of design parameters and 3D-printing orientation to enhance the efficiency of topology-optimized components in additive manufacturing. *Results Mater.* **26**, 100702 (2025).
19. Efa, D. A., Gutema, E. M., Lemu, H. G. & Gopal, M. Optimization of titanium alloy-Ti-6Al-4V to minimize mass, maximize stiffness and frequency in additive manufacturing. *Key Eng. Mater.* **980**, 3–13 (2024).
20. Wen, P., Zhang, B., Li, C., Duan, Y. & Li, H. A unified DQFE framework for size-dependent vibration of multi-layered microplate systems with elastic boundary conditions and interlayer coupling. *Thin-Walled Struct.* **222**, 115019 (2026).
21. Li, X., Xie, M., Feng, J. & Hu, Y. Magnetoelastic free vibration of a microplate on an elastic foundation. *Thin-Walled Struct.* **224**, 114652 (2026).
22. Nikbakht, I., Hamzehei-Javaran, S. & Shojaee, S. New insight into the analysis of size-dependent higher-order microplates with modified strain gradient finite elements. *J. Eng. Mech.* **151**, 04025078 (2025).
23. Tounsi, A. et al. Quasi-3D plate theory for size-dependent static and free vibration analysis of FG microplate with porosities based on a modified couple stress theory. *Mech. Adv. Mater. Struct.* **33**(1), 2463687 (2025).
24. He, G., Li, Z., Gui, H. & Cao, D. Dynamic modeling and nonlinear vibrations of a rotating poly-crystalline silicon microplate based on the modified couple stress theory. *Eur. J. Mech. ASolids* **115**, 105833 (2025).
25. Wang, W. & He, T. Thermoelastic damping analysis to CNTs and GPLs reinforced FG microplate based on nonlocal strain gradient theory and nonlocal dual-phase-lag heat conduction model. *Appl. Phys. A* **131**, 1–26 (2025).
26. Wang, J., Liou, S., Qu, S., Liang, H. & Yu, Y. Study on the scale effect of nonlinear vibration of axial motion micro/nano plates based on nonlocal strain gradient theory. *Mech. Solids* **60**, 3145–3167 (2025).
27. Wu, C.-P. & Chang, T.-Y. A review of modified/consistent couple stress and strain gradient theories for analyzing static and dynamic behaviors of functionally graded microscale plates and shells. *Materials* **18**, 4475 (2025).
28. Song, W., Li, R., Feng, G. & Xiao, L. Dynamic mechanical behaviors and deformation mechanism of hybrid triply periodic minimal surface structures. *Int. J. Impact Eng.* **203**, 105359 (2025).
29. Nguyen, N. V. & Nguyen, S. H. Dynamic instability analysis of nature-inspired lattice microplates reinforced with graphene: NV Nguyen, SH Nguyen. *Arch. Appl. Mech.* **95**, 115 (2025).
30. Chen, L., Deng, Y., Yaylaci, M. & Safarpour, M. Hybrid computational framework for nonlinear dynamic analysis of polygonal FG-PET-TPMS plates used in future walking sport tracks via refined theories FEM, and deep learning. *Thin-Walled Struct.* **226**, 114714 (2026).
31. Tran, V.-T., Nguyen, T.-K., Wattanasakulpong, N. & Vo, T. P. Stochastic Chebyshev-Ritz analysis of size-dependent GPLR-FG-TPMS microplates using polynomial chaos with bi-directional deep neural network. *Mech. Based Des. Struct. Mach.* **54**, 2695183 (2026).
32. Dong, D. T., Minh, T. Q., Tu, B. T., Tran, K. Q. & Nguyen-Xuan, H. Nonlinear thermo-mechanical static stability analysis of FG-TPMS shallow spherical shells. *Thin-Walled Struct.* https://doi.org/10.1016/j.tws.2024.112343 (2024).
33. Nguyen-Xuan, H., Tran, K. Q., Thai, C. H. & Lee, J. Modelling of functionally graded triply periodic minimal surface (FG-TPMS) plates. *Compos. Struct.* **315**, 116981. https://doi.org/10.1016/j.compstruct.2023.116981 (2023).
34. Nguyen, N. V., Tran, K. Q., Lee, J. & Nguyen-Xuan, H. Nonlocal strain gradient-based isogeometric analysis of graphene platelets-reinforced functionally graded triply periodic minimal surface nanoplates. *Appl. Math. Comput.* **466**, 128461 (2024).
35. Gibson, L. J. Cellular solids. *Mrs Bull.* **28**, 270–274 (2003).
36. Wenham, S. R. & Green, M. A. Silicon solar cells. *Prog. Photovolt. Res. Appl.* **4**, 3–33 (1996).
37. Lam, D. C., Yang, F., Chong, A., Wang, J. & Tong, P. Experiments and theory in strain gradient elasticity. *J. Mech. Phys. Solids* **51**, 1477–1508 (2003).
38. Zhang, W. et al. Nonlinear resonant responses of a novel FGM sandwich cylindrical shell structure for supersonic flight vehicles based on 1:1 internal resonance between conjugate modes. *Aerosp. Sci. Technol.* **152**, 109372. https://doi.org/10.1016/j.ast.2024.109372 (2024).
39. Aboutalebi, R. Three-dimensional flutter analysis of a novel circular sandwich plate employing hyperbolic shear deformation theory. *Aerosp. Sci. Technol.* **150**, 109223. https://doi.org/10.1016/j.ast.2024.109223 (2024).
40. Mohammadi, R. & Hosseini, M. Modeling and free vibration analysis of a rotating functionally graded thin-walled hub-blade system under aerothermoelastic loading. *Aerosp. Sci. Technol.* **146**, 108935. https://doi.org/10.1016/j.ast.2024.108935 (2024).
41. Riccio, A., Caprio, F. D., Tsai, S. W., Russo, A. & Sellitto, A. Optimization of composite aeronautical components by re-designing with double-double laminates. *Aerosp. Sci. Technol.* **151**, 109304. https://doi.org/10.1016/j.ast.2024.109304 (2024).
42. Shabani, P., Li, L., Laliberte, J. & Qi, G. Enhanced LaRC05 failure criteria for investigating low-velocity impact on fiber-reinforced composites: An experimental and computational study. *Aerosp. Sci. Technol.* **155**, 109554. https://doi.org/10.1016/j.ast.2024.109554 (2024).
43. Oñate, E. *Structural Analysis with the Finite Element Method. Linear Statics: Volume 2: Beams, Plates and Shells* (Springer Science & Business Media, 2013).
44. Krack, M. & Gross, J. *Harmonic Balance for Nonlinear Vibration Problems* (Springer, 2019).
45. Ferreira, J. V. & Serpa, A. L. Application of the arc-length method in nonlinear frequency response. *J. Sound Vib.* **284**, 133–149 (2005).
46. Thai, S., Thai, H.-T., Vo, T. P. & Patel, V. I. Size-dependant behaviour of functionally graded microplates based on the modified strain gradient elasticity theory and isogeometric analysis. *Comput. Struct.* **190**, 219–241 (2017).
47. Thai, H.-T. & Choi, D.-H. Size-dependent functionally graded Kirchhoff and Mindlin plate models based on a modified couple stress theory. *Compos. Struct.* **95**, 142–153. https://doi.org/10.1016/j.compstruct.2012.08.023 (2013).

Acknowledgements

This work was supported by the Science and Technology Research Program of Chongqing Municipal Education Commission (Grant No. KJZD-K202502903) and the Chongqing Preschool Education College Scientific Research Platform in 2024. Project name: Digital Elderly Care Service Big Data Application Research Center (Grant Number: 2024KYPT-01).

Author contributions

Dr. Long Liu [Author 1]: Conceptualization; Software; Methodology; Validation; Formal Analysis; Investigation; Writing – Original Draft; Writing – Review & Editing. Contributed extensively to recoding major parts of the computational framework, numerical verification, implementation of reviewer-requested revisions, and substantial rewriting of the manuscript. Dr. Jalil jamali [Author 2]: Software; Validation; Formal Analysis; Investigation; Data Curation; Writing – Review & Editing. Contributed significantly to code development, numerical validation, correction of technical issues, response to reviewer comments, and revision of major sections of the manuscript. Dr. Loke Kok Foong [Author 3]: Methodology; Formal Analysis; Investigation; Writing – Review

& Editing, correction of technical issues, response to reviewer comments, and revision of major sections of the manuscript. Dr. Murat Yaylacı [Author 4]: Validation; Formal Analysis; Resources; Writing – Review & Editing, implementation of reviewer-requested revisions, and substantial rewriting of the manuscript. All authors reviewed the manuscript, approved the final version, and agreed to be accountable for all aspects of the work.

Funding
There was no Funding.

Additional information
Correspondence and requests for materials should be addressed to J.j. or L.K.F.

Reprints and permissions information is available at www.nature.com/reprints.

Publisher's note Springer Nature remains neutral with regard to jurisdictional claims in published maps and institutional affiliations.

Open Access This article is licensed under a Creative Commons Attribution-NonCommercial-NoDerivatives 4.0 International License, which permits any non-commercial use, sharing, distribution and reproduction in any medium or format, as long as you give appropriate credit to the original author(s) and the source, provide a link to the Creative Commons licence, and indicate if you modified the licensed material. You do not have permission under this licence to share adapted material derived from this article or parts of it. The images or other third party material in this article are included in the article's Creative Commons licence, unless indicated otherwise in a credit line to the material. If material is not included in the article's Creative Commons licence and your intended use is not permitted by statutory regulation or exceeds the permitted use, you will need to obtain permission directly from the copyright holder. To view a copy of this licence, visit http://creativecommons.org/licenses/by-nc-nd/4.0/.

© The Author(s) 2026